

1 **Time-resolved *in situ* synchrotron-microCT: 4D deformation**
2 **of bone and bone analogues using digital volume**
3 **correlation**
4
5
6
7
8
9

10 5 Marta Peña Fernández ^{1,2,*}, Alexander P. Kao ¹, Roxane Bonithon ¹, David
11 Howells ³, Andrew J. Bodey ⁴, Kazimir Wanelik ⁴, Frank Witte ^{5,6}, Richard
12 Johnston ³, Hari Arora ³, Gianluca Tozzi ¹
13
14
15

16
17 1. Zeiss Global Centre, School of Mechanical and Design Engineering, University of
18 Portsmouth, Portsmouth, UK.
19

20
21 10 2. School of Engineering and Physical Sciences, Heriot-Watt University, Edinburgh, UK.
22

23 3. Faculty of Science and Engineering, Swansea University, Swansea, UK.
24

25 4. Diamond Light Source, Oxfordshire, UK.
26

27 5. Biotrics Bioimplants AG, Berlin, Germany.
28

29 15 6. Department of Prosthodontics, Geriatric Dentistry and Craniomandibular Disorders,
30 Charité - Universitätsmedizin Berlin, Berlin, Germany.
31

32
33
34
35
36 *Corresponding author:

37 Marta Peña Fernández, PhD
38

39 20 Heriot-Watt University
40

41 School of Engineering and Physical Sciences (EPS)
42

43 Institute of Mechanical, Process and Energy Engineering (IMPEE)
44

45 James Nasmyth Building, Room JN 2.24
46

47 Edinburgh, EH14 4AS, UK
48

49 25 Email: M.Pena_Fernandez@hw.ac.uk
50
51
52
53
54
55
56
57
58
59
60
61
62
63
64
65

Abstract

Digital volume correlation (DVC) in combination with high-resolution micro-computed tomography (microCT) imaging and *in situ* mechanical testing is gaining popularity for quantifying 3D full-field strains in bone and biomaterials. However, traditional *in situ* time-lapsed (i.e., interrupted) mechanical testing cannot fully capture the dynamic strain mechanisms in viscoelastic biological materials. The aim of this study was to investigate the time-resolved deformation of bone structures and analogues via continuous *in situ* synchrotron-radiation microCT (SR-microCT) with compression and DVC to gain a better insight into their structure-function relationships. Fast SR-microCT imaging enabled the deformation behaviour to be captured with high temporal and spatial resolution. Time-resolved DVC highlighted the relationship between local strains and damage initiation and progression in the different biostructures undergoing plastic deformation, bending and/or buckling of their main microstructural elements. The results showed that SR-microCT continuous mechanical testing complemented and enhanced the information obtained from time-lapsed testing, avoiding the inherent relaxation behaviour of porous viscoelastic biomaterials in between steps, which may underestimate the 3D strain magnitudes. Altogether, the findings of this study highlight the importance of time-resolved *in situ* experiments to fully characterise the time-dependent mechanical behaviour of biological tissues and biomaterials and to further explore their micromechanics under physiologically relevant conditions.

Keywords: Bone, time-resolved SR-microCT, continuous *in situ* mechanics, digital volume correlation, time-dependent behaviour.

1. Introduction

Biological materials, such as bone, as well as novel synthetic bioinspired foams and scaffolds, present complex heterogeneous, anisotropic and hierarchical structures [1–5]. Therefore, their mechanical behaviour is largely governed not only by their intrinsic material properties but also by their arrangement and distribution at different length scales [6–12]. At the mesoscale, trabecular and cortical bone mechanics mostly depend on the mineral density distribution and microarchitecture (i.e. porosity, orientation)[13–15], and thus a thorough characterization of the local mechanical properties at trabecular or osteonal level is needed in order to evaluate the effect of altered bone microstructure due to different musculoskeletal pathologies, such as osteoporosis or bone cancer, on the risk of fracture or the outcome of treatments and therapies [16–18]. On the other hand, engineered biomaterials are under constant development aiming to replicate the mechanical behaviour and morphology of bone by either acting as bone surrogates to evaluate the performance of medical implants and devices [19,20] or as scaffolds to treat critical-sized defects following disease or trauma [21]. Either way, these biostructures need to provide appropriate mechanical integrity both as a whole construct and locally to ensure a successful outcome. A deep understanding on the relationships between complex three-dimensional (3D) microstructures and local mechanics in bone and biostructures is, therefore, essential.

To date, the only experimental technique that allows for 3D local strain measurements within bone and biostructures is digital volume correlation (DVC) based on 3D imaging techniques such as X-ray micro-computed tomography (microCT) and concomitant *in situ* mechanics. Indeed, high-resolution microCT remains the main imaging modality used in the development of DVC [22–24], and it has been widely used to study the deformation of hard and soft biological tissues [25–29], as well as complex bone-biomaterial systems [30,31]. Traditionally, *in situ* microCT mechanical testing is performed in a stepwise manner, also known as time-lapsed testing, where loading is applied to the structures in discrete steps, each followed by a full tomographic acquisition after stress relaxation is stabilised [32,33]. However, all biomaterials exhibit a time-dependent mechanical behaviour which, in living tissues, plays a critical role in physiological activities [34]. Bone, for example, is a well-known viscoelastic tissue that exhibits frequency-dependent damping, stress relaxation and creep behaviour even at small load levels [35–38]. Therefore, DVC analysis based on time-lapsed tests cannot be used to capture the physiological strain mechanisms in biological materials, as their time-dependent response may alter the local measured strains. Thus, it is necessary to simultaneously measure local mechanical properties and directly quantify microstructural evolution with time in order to assess the dynamic deformation of bone and biomaterials.

1
2
3 85 *In situ* experiments performed in conventional laboratory-based microCT systems usually
4 require long times for high-resolution image acquisition, hence time-lapsed testing remains
5 the most viable procedure [39,40]. Although new systems and protocols are being developed
6 providing higher temporal and spatial resolution microCT imaging in lab-based facilities [41–
7 44], their application is certainly new, and the limited X-ray flux produced by micro-focused X-
8 ray tubes demands an acceptable trade-off between noise and motion blurring when following
9 a dynamic process [40,41]. Despite those disadvantages, Kytýř et al. [42] operated an in-
10 house microCT system to investigate the deformation of porous hydrogel-based scaffolds
11 90 during continuous *in situ* compression using DVC. However, the achieved spatial and temporal
12 resolution were limited to ~30 μm and 120 s, respectively, and thus uniaxial compression was
13 carried out at a considerably low loading rate of 0.4 μm / s to minimise motion artefacts [42].
14 On the other hand, the high flux of synchrotron X-ray radiation enables microCT images to be
15 acquired with high signal-to-noise ratio (SNR) at high temporal and spatial resolution, and
16 consequently, it allows the characterization of dynamic processes within 3D microstructures
17 [45–47]. As such, time-resolved synchrotron experiments have been carried out over the past
18 years to investigate the *in situ* sintering of ceramic materials [47–49], the underlying physics
19 of laser additive manufacturing process [50] as well as the deformation of semi-solid metals
20 95 subjected to uniaxial compression [51–53] and indentation [54] among other applications. To
21 such extent, Cai et al. [52,54] made use of DVC to quantify the strain localization in a semi-
22 solid alloy during continuous *in situ* SR-microCT compression [52] and indentation [54] with
23 full tomographic datasets acquired in 4 and 9 s, and at 12.2 and 4 μm resolution, respectively,
24 allowing the identification of dilatant shear bands during real-time compression and plastic
25 deformation as well as compaction of individual grains during indentation. More recently, Peña
26 Fernández et al. [55] explored the use of continuous *in situ* SR-microCT mechanics and DVC
27 to investigate the effect of damage accumulation due to cyclic loading on the overall fracture
28 100 outcome of cortical bone specimens, showing a decrease of the strain magnitudes prior to
29 failure with the number of applied cycles. However, only the post-cyclic failure behaviour of
30 cortical bone was evaluated, but a full characterisation of the structure-function relationships
31 during the dynamic deformation of intact bone and biomaterials under mechanical loads was
32 not addressed.
33
34
35
36 105
37
38
39
40
41
42
43
44
45 110
46
47
48
49
50

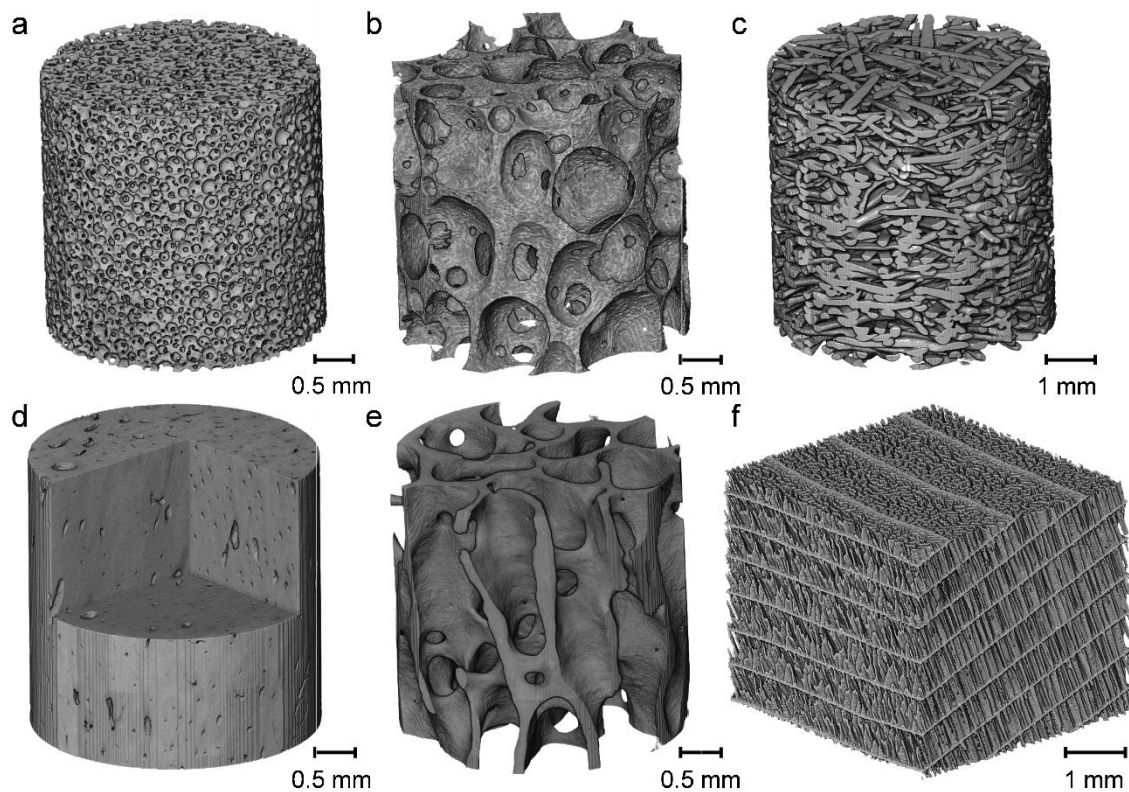
51 Therefore, the main aim of this study was to investigate, for the first time, the time-resolved
52 deformation of a variety of bone structures (trabecular and cortical bone as well as cuttlebone)
53 and analogues (synthetic foams and Mg-based scaffolds), using continuous *in situ* SR-
54 115 microCT with uniaxial compression and DVC. The SR-microCT imaging acquisition
55 parameters were fine-tuned for each biostructure allowing resolution of their main features of
56 interest, and a comparison of the local DVC-computed strain fields based on SR-microCT
57
58
59
60
61
62
63
64
65

1
2 120 images acquired under both continuous and time-lapsed loading was carried out on the
3 synthetic bone surrogates, due to their overall consistency in mechanical behaviour. Finally,
4 the dynamic full-field strain distribution in all biostructures was evaluated over time **in relation**
5 **to, or as a joint contribution of, their microstructural changes and associated to damage**
6 **initiation and propagation**. The findings of this article will be of fundamental importance in
7 establishing new guidelines for *in situ* time-resolved SR-microCT experiments of biomaterials,
8 particular those showing high viscoelasticity and time-dependent mechanical behaviour.
9
10 125

11 2. Materials and methods

12 2.1. Specimens

13
14 A variety of materials, both synthetic and biological, were sourced to investigate the capability
15 of the method in capturing the time-resolved deformation of biostructures with diverse
16 morphology (Figure 1). This included synthetic foams, Mg-based open porous scaffolds,
17 bovine trabecular and cortical bone as well as cuttlebone.
18
19 130
20
21
22
23
24
25



26
27
28
29
30
31
32
33
34
35
36
37
38
39
40
41
42
43
44
45
46
47
48
49
50
51
52
53
54
55 135 Figure 1. Reconstructed SR-microCT volumes of the specimens tested. (a) Closed-cell foam (Sawbones PCF20),
56 (b) open-cell foam (Sawbones PCF15), (c) Mg-based open porous scaffold (d) cortical bone, (e) trabecular bone
57 and (f) cuttlebone. **SR-microCT images were acquired with a (a, b, d, e) 6.5 μm , (c) 10.4 μm and (e) 5.2 μm isotropic**
58 **voxel size.**
59

60 2.1.1. Synthetic foams

1
2 140 Closed-cell and open-cell foams (PCF20 and PCF15, Sawbones, Pacific Research
3 Laboratories, WA, USA) were selected to represent bone microstructure with controlled
4 mechanical and morphological properties. Cylindrical samples (6 mm diameter, 16 mm length)
5 were extracted from Sawbones blocks (n = 6 per group) with a carbons steel drill bit and
6 mounted on brass endcaps to achieve a final free length of 12 mm (2:1 aspect ratio), reducing
7 experimental artefacts during mechanical testing [56].
8
9

10 145 2.1.2. Mg-based scaffolds.

11
12 Mg-based open porous scaffolds (Biotrics Bioimplants AG, Berlin, Germany) produced by
13 liquid-phase sintering and designed for bone replacement were also investigated [4]. This
14 material was of interest due to its higher ductility but similar strut thickness to trabecular bone.
15 Furthermore, being a non-biological material, any possible radiation-induced damage can be
16 neglected [57,58]. Cylindrical samples (n = 3, 8 mm diameter, 20 mm length) were embedded
17 into acetal endcaps to achieve a 10 mm final free length and to ensure perpendicularity
18 between the scaffold's main axis and base.
19
20 150

21 2.1.3. Trabecular and cortical bone.

22
23 Trabecular and cortical bone specimens were obtained from a fresh-frozen bovine tibial
24 condyle and mid femoral diaphysis, respectively. Cylindrical plugs (6 mm for trabecular and 4
25 mm diameter for cortical bone, ~ 20 mm length) were cored in the proximal-distal direction
26 using a trephine blur drill under constant water irrigation. The ends of the specimens were
27 then trimmed plane and parallel with a bandsaw to achieve 14 mm length for trabecular and
28 10 mm length for cortical bone. All specimens were wrapped in gauze, soaked in phosphate
29 buffered saline (PBS) and stored at -20°C until testing. Prior to the experiment, the ends of
30 the specimens were cleaned, dried and embedded into brass endcaps using a custom-made
31 alignment jig, achieving a nominal final free length of 12 mm and 8 mm (2:1 ratio) for trabecular
32 and cortical bone, respectively [56].
33
34
35
36
37
38 160
39
40
41
42
43
44

45 2.1.4. Cuttlebone

46
47 165 Fresh specimens of *Sepia officinalis* Linnaeus, 1758, were acquired commercially from
48 around the UK coastline and stored at -20°C. Several days prior to imaging, the cuttlebone
49 was dissected from the organism, immersed in PBS, and stored in an airtight container.
50 Several hours prior to imaging the cuttlebone was sectioned using a handheld rotary cutting
51 disk into smaller cubic samples (approximately 5 x 5 x 5 mm) taken from near the central
52 region of the cuttlebone, not including any of the dorsal shield material, and allowed to dry
53 prior to testing.
54
55
56 170
57
58
59

60 2.2. Image acquisition.

SR-microCT was performed at the Diamond-Manchester Imaging Branchline I13-2 [59] of Diamond Light Source, UK. A partially coherent polychromatic ‘pink’ beam (8–30 keV) of parallel geometry was generated by an undulator from an electron storage ring of 3.0 GeV. The undulator gap was set to 5 mm for data collection and, to limit bone damage, 11 mm for low-dose alignment. The beam was reflected from the platinum stripe of a grazing-incidence focusing mirror and high-pass filtered with 1.4 mm pyrolytic graphite, 3.2 mm aluminium and 60 µm steel. Images were recorded by a sCMOS (2560 × 2160 pixels) pco.edge 5.5 (PCO AG, Germany) detector which was coupled to a visual light microscope with various objective lenses; 500 µm thick CdWO₄ and LuAG:Ce scintillators were used with the 1.25x and 2x objective lenses, respectively, leading to a field of view of 6.7 x 5.6 mm for the 1.25x lens and 4.2 x 3.5 mm for the 2x lens. On-chip pixel binning was used to improve the signal-to-noise ratio and facilitate faster framerates. Imaging settings were optimised for each specimen type and are summarized in Table 1.

Table 1. Summary of imaging settings used for the acquisition of SR-microCT images for each material type, including closed-cell (PCF20) and open-cell (PCF15) polyurethane foam, Mg-based open porous scaffold (Mg), trabecular bone (TB), cortical bone (CB) and cuttlebone (CF, cuttlefish bone). n: number of specimens tested per material type.

Material	n	Lens	Binning	Nominal voxel size (µm)	Projections	Exposure time (ms)	Read-out time (ms)
PCF20	6	2x	4	6.5	1201	9	2
PCF15	6	2x	4	6.5	1201	9	2
Mg	3	1.25x	4	10.4	1441	8	4
TB	5	2x	4	6.5	1201	15	3.5
CB	4	2x	4	6.5	1201	10	3.5
CF	1	1.25x	2	5.2	1201	10	2

Projection images were acquired over 180° of continuous rotation (‘fly scan’). The compression rig was not moved between scans. The average delay between two sequential scans was approximately 11 s, as estimated from the timestamps of the generated files. Prior to reconstruction, the projection images were flat- and dark-field corrected. For each specimen, 40 flat- and dark-field images were collected before and after the scan series, to account for possible variations during the experiment. Flat-field images were collected with

1 the compression rig in place, but the specimen absent. A filtered back projection algorithm
2 was used for reconstruction of the 3D datasets in Savu [60,61], which incorporated a fast ring
3 artefact suppression algorithm based on the work of Titarenko et al. [62] and zingers removal.

4
5 200 The specific plugins and parameters used during reconstruction are specified in Table S1.

6
7 For trabecular and cortical bone specimens, the radiation dose was estimated as in [58],
8 assuming the same photon energy and flux (28.93 keV and 4.9×10^{13} photons/s, as estimated
9 using SPECTRA code [63]). Specimens were considered as homogeneous cylinders with
10 apparent densities of 0.55 g/cm³ for trabecular [64] and 1.92 g/cm³ for cortical bone [65]. A
11 mass attenuation coefficient of 1.53 cm²/g [66] was used for both cortical and trabecular bone,
12 as it was previously shown to describe well the absorption profile simulated in the same
13 experimental setup using FLUKA Monte Carlo [58]. This resulted in an estimated dose rate of
14 205 34.81 Gy/s and 45.27 Gy/s for cortical and trabecular bone specimens, respectively. The total
15 radiation dose absorbed for each specimen is specified in Table S2, and it remained below
16 20.1 kGy for all specimens. The cuttlebone was tested in a different setup (i.e., loading stage),
17 thus an estimation of the absorbed dose could not be conducted with the available data.

26 2.3. *In situ* mechanics.

27
28 *In situ* uniaxial compression testing was performed via a micro-mechanical testing device
29 equipped with a 5kN load cell (CT5000, Deben Ltd, UK) on all specimens but the cuttlefish
30 bone, which was tested in a 500 N load cell device (CT500, Deben Ltd, UK). Synthetic bone
31 models, trabecular and cortical bone were placed within an environmental chamber and
32 215 immersed in PBS solution throughout the duration of the test, whereas Mg-based scaffolds
33 and cuttlebone were tested in dry conditions. All tests were carried out under displacement
34 control at a constant crosshead speed of 0.1 mm/min. The total amount of compression for
35 each specimen during a full tomogram acquisition is reported in Table S3.

36
37 For all specimens, a small preload (~2 - 10 N) was first applied to ensure good end contact
38 prior to testing and two repeated tomographic datasets were acquired for DVC error analysis
39 [24]. Synthetic bone models were divided into two groups (n = 3 per type/group) to allow a
40 225 direct comparison of the deformation in the specimens during time-lapsed or continuous test.
41 Half of the synthetic bone models were subjected to time-lapsed *in situ* mechanics at three
42 compression levels (1%, 2% and 3% apparent strain). At each step, specimens were allowed
43 to settle for 10 minutes before image acquisition to reduce stress relaxation during imaging,
44 and full tomographic datasets were then acquired under the applied compression. Continuous
45 loading was performed in all other specimens at a constant speed of 0.1 mm/min, with images
46 230 acquired uninterruptedly during compression up to apparent failure (i.e., structural collapse or
47
48
49
50
51
52
53
54
55
56
57
58
59
60
61
62
63
64
65

high densification). Therefore, the total number of full consecutive tomographic datasets collected was specimen dependent and are reported in Table S3.

2.4. Image postprocessing.

Following image acquisition and reconstruction, the 3D SR-microCT images for each specimen were rigidly registered using the first preloaded image as a reference [23]. Registration was performed with dedicated Matlab (v2018a, MathWorks, Natick, MA, USA) scripts. Prior to registration, images were converted from 32-bit to 16-bit. Mattes mutual information algorithm [67] was used as a similarity metric and one-plus-one evolutionary configuration [68] was employed for optimising the image metric, with an initial and minimum size of the search radius of 10^{-5} and 1.5×10^{-6} , respectively, a growth factor of the search radius of 1.05, and a maximum number of iterations of 100. After rigid alignment of the 3D datasets, images were denoised in Matlab using an anisotropic diffusion filter, where the gradient threshold and number of iterations were estimated using Matlab in-built function *imdiffusest* on the centre-slice of each specimen [69,70]. Finally, a volume of interest (VOI) was selected for each specimen as the volume of material present on both the first and last acquired tomograms.

The filtered images were segmented using the pixel classification workflow available in ilastik (V1.3.0) [71]. For each specimen, six scans were selected, and the central 20 slices were used to train the classifier and segment each volumetric image into two classes (i.e., solid materials and background). The model was trained computing different features (i.e., Gaussian smoothing, Laplacian of Gaussian, Gaussian Gradient Magnitude, Difference of Gaussians, Structure Tensor Eigenvalues and Hessian of Gaussian Eigenvalues) in 3D at five σ values ($\sigma = 0.3, 0.7, 1.0, 1.6, 3.5$) and in 2D with $\sigma = 5.0$. The segmented images of the first acquired dataset (i.e., preload configuration) for each specimen was used for a morphological analysis. The solid volume fraction (SV_f) was computed for each specimen as the volume of solid material over the entire VOI. Additionally, mean strut thickness and spacing in synthetic bone models, mean fibre thickness and spacing in Mg-based scaffolds, mean trabecular thickness and spacing in trabecular bone specimens, mean canal thickness and spacing in cortical bone specimens and mean pillar thickness and spacing in cuttlebone chamber were computed using BoneJ [72] plugin in FIJI [73]. For Mg-based scaffolds, the evolution of the fibre spacing during compression was also analysed.

2.5. Digital volume correlation (DVC).

DVC (DaVis v10.05, LaVision, Germany) analysis was performed to evaluate the 3D full-field strains of all specimens and quantify their dynamic deformation. The DaVis software is based on a local approach of deformable registration and further details on the operating principles

of the algorithm are detailed elsewhere [74,75]. Briefly, the measurement volumes (i.e., 3D image) are divided into smaller subvolumes and the matching between the reference and deformed images is achieved via a direct cross-correlation function of the gray-levels, which is preceded by a Fast Fourier Transform (FFT)-based correlation to initialise the computation. The DaVis software adopts a multipass scheme that uses the displacement gradient from a previous pass to deform the subvolume on the subsequent pass until the highest possible correlation is achieved.

The acquired preloaded repeated scans were used to evaluate displacement precision and strain uncertainties (i.e., mean absolute strain error (MAER) and standard deviation of the error (SDER), also known as accuracy and precision, respectively) [76] using ten different multipass schemes with final subvolumes ranging from 8 to 80 voxels (see Table S5, Fig S1, S2). No overlap between subvolumes was used, meaning each subvolume did not share any gray-scale pattern with their neighbouring one in the correlation procedure. The final DVC-schemes used for each material and the corresponding displacement and strain errors are summarized in Table 2. Such schemes then allowed to evaluate the 3D full-field strain distribution in the specimens over time (i.e., four-dimensional (4D) evaluation) in relation to the deformation induced by the compressive applied load.

Table 2. Summary of DVC multipass scheme used for each material and corresponding displacement and strain errors for the n number of specimens analysed for closed-cell (PCF20) and open-cell (PCF15) polyurethane foam, Mg-based open porous scaffold (Mg), trabecular bone (TB), cortical bone (CB) and cuttlebone (CF, cuttlefish bone). Errors are reported as mean (standard deviation) for both MAER and SDER among the n specimens per material.

Material	n	DVC multipass scheme (voxel)	Subvolume size (μm)	Displacement precision (μm) ^b	MAER ($\mu\epsilon$)	SDER ($\mu\epsilon$)
PCF20	6	128 ^a -64-56-48-40	260.0	0.49 (0.35)	348 (179)	134 (39)
PCF15	6	128 ^a -64-56-48-40	260.0	0.73 (0.36)	247 (152)	132 (66)
Mg	3	160 ^a -80-72-64-56	364.0	1.01 (0.55)	540 (306)	284 (234)
TB	5	144 ^a -72-64-56-48	312.0	0.72 (0.35)	490 (226)	210 (84)
CB	4	144 ^a -72-64-56-48	312.0	0.84 (0.22)	411 (113)	252 (113)
CF	1	96 ^a -48-40-32-24	124.8	0.03	19	10

^a FFT pre-shift windows size preceding multi-pass direct correlation DVC computation.

^b Highest value of displacement precision among the three displacement components is reported.

3. Results

The sourced materials used in this study presented a clearly characteristic microstructure (Figure 1) as highlighted by the morphological analysis (Table 3), with solid volume fractions ranging from 16.9% for the cuttlebone to 96.9% in cortical bone specimens, the most and least porous specimen, respectively. The non-biological materials (i.e., PCF15, PCF20 and Mg specimens) showed a smaller intra-specimen variation in all the measured morphometric parameters compared to trabecular and cortical bone specimens. Synthetic bone models exhibited comparable porosity to trabecular bone specimen. The thinnest analysed structures corresponded to the 25.7 μm -thick pillars in the cuttlebone chamber, 42.5 μm -thick walls in the closed-cell foam PCF20 and 83.6 μm -thick canals in cortical bone specimens. Trabecular bone, open-cell foam PCF15 and Mg-scaffolds displayed a similar thickness.

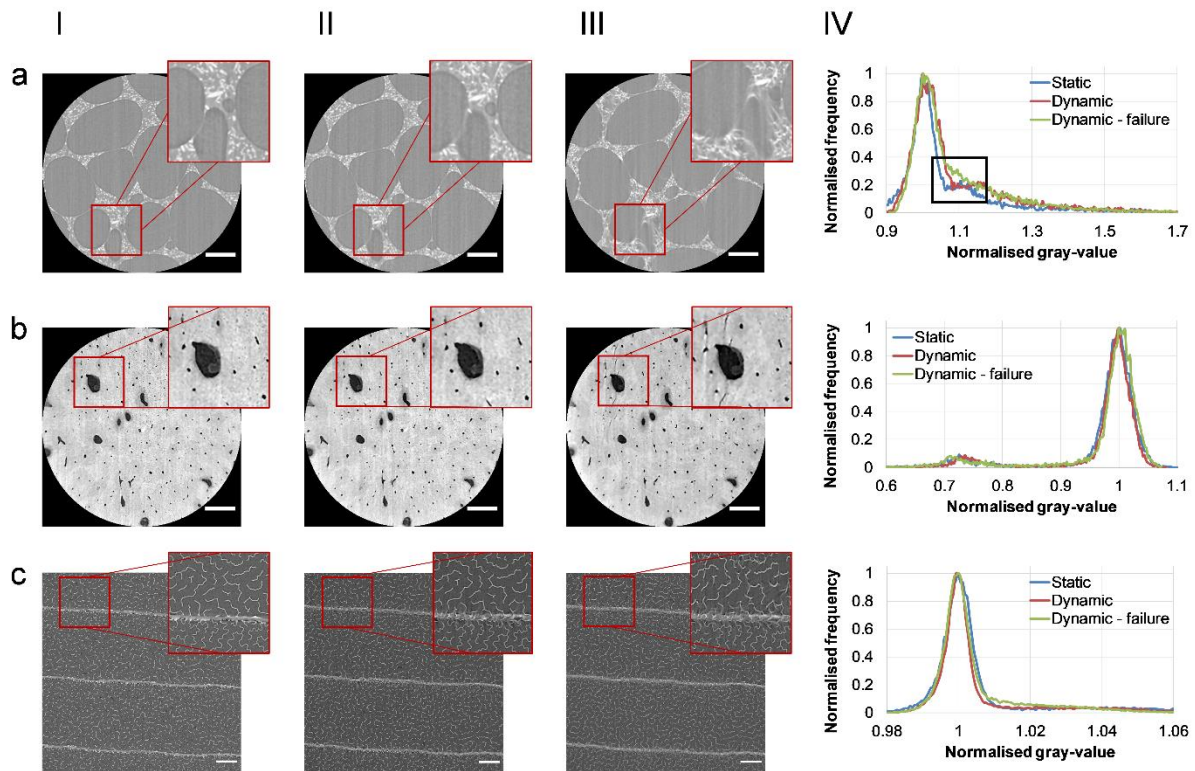
Table 3. Summary of the morphological parameters of the analysed biostructures including closed-cell (PCF20) and open-cell (PCF15) polyurethane foam, Mg-based open porous scaffold (Mg), trabecular bone (TB), cortical bone (CB) and cuttlebone (CF, cuttlefish bone). For each material, solid volume fraction (SV_f), thickness and spacing are reported as mean (standard deviation) among the n specimens per material.

Material	n	SV_f (%)	Thickness (μm)	Spacing (μm)
PCF20	6	26.4 (1.1)	42.5 (1.4)	170.8 (4.9)
PCF15	6	22.8 (1.4)	139.9 (4.5)	741.6 (60.1)
Mg	3	42.8 (1.0)	143.7 (1.2)	220.0 (8.3)
TB	5	21.7 (6.3)	179.0 (35.7)	654.3 (33.9)
CB	4	96.9 (0.3)	83.6 (15.8) ^a	323.9 (43.7) ^a
CF	1	16.9	25.7	101.4

^a Thickness and spacing of cortical bone Haversian and Volkmann canals.

The optimisation of the imaging settings allowed to resolve the main features of interest in each material for both static and dynamic conditions (Figure 2-I,II). A qualitative inspection of

1
2
3 310 the SR-microCT images demonstrated that the smallest details in the biostructures, such as
4 the structural fillers in the open-cell foam (PCF15), the thinnest vascular canals in cortical
5 bone and the pillars in the cuttlebone, were not affected by motion artefacts during dynamic
6 imaging (Figure 2-II) with the exception of regions where failure occurred due to the applied
7 compression (Figure 2-III). This was also observed as a small shift in the image histograms
8 (Figure 2-IV), and it was more evident for the cellular foam (PCF15), for which the contrast
9 between the fillers and matrix was partially lost (Figure 2a-III,IV).



10
11
12
13
14
15
16
17
18
19
20
21
22
23
24
25
26
27
28
29
30
31
32
33
34
35
36
37 315
38
39 Figure 2. Analysis of SR-microCT images acquired during static and dynamic conditions. A representative SR-
40 microCT cross-section is shown for (a) open-cell foam PCF15, (b) cortical bone and (c) cuttlebone while imaging
41 was performed statically (I), and dynamically during the linear loading regime (II) and mechanical failure (III). (IV)
42 Normalised histograms of the zoomed-in regions in (I-III). Normalisation was performed with respect to the mode
43 (e.g., most frequent) values of each histogram. Scale bars: 500 μm .
44
45 320

46
47 The apparent mechanical behaviour of the closed-cell foam (PCF20) was fairly consistent for
48 all specimens, showing an initial elastic range up to $\sim 2\text{-}3\%$ deformation followed by strain
49 hardening period in which pores started to collapse (Figure 3a). Stress-relaxation was visible
50 for specimens subjected to time-lapsed compression at the end of each step, when the
51 actuator was stopped, and specimens were allowed to settle before image acquisition. DVC-
52 computed third principal strains (i.e., ϵ_{p3}) increased linearly with the applied compression, with
53 specimens tested dynamically experiencing approximately two-fold local strain in average
54 325
55 computed third principal strains (i.e., ϵ_{p3}) increased linearly with the applied compression, with
56 specimens tested dynamically experiencing approximately two-fold local strain in average
57 (Figure 3b). The 3D full-field ϵ_{p3} revealed local strain accumulation in the centre of the
58
59
60
61
62
63
64
65

specimens, as the pores in the solid foam matrix closed due to the applied deformation (Figure 3c). Off-axis compression was detected in PCF20#2 and PCF20#6, which showed maximum strain levels accumulating on one side of the volume and higher heterogeneity in the strain distribution at each step (Figure 3b, Video S1,S2).

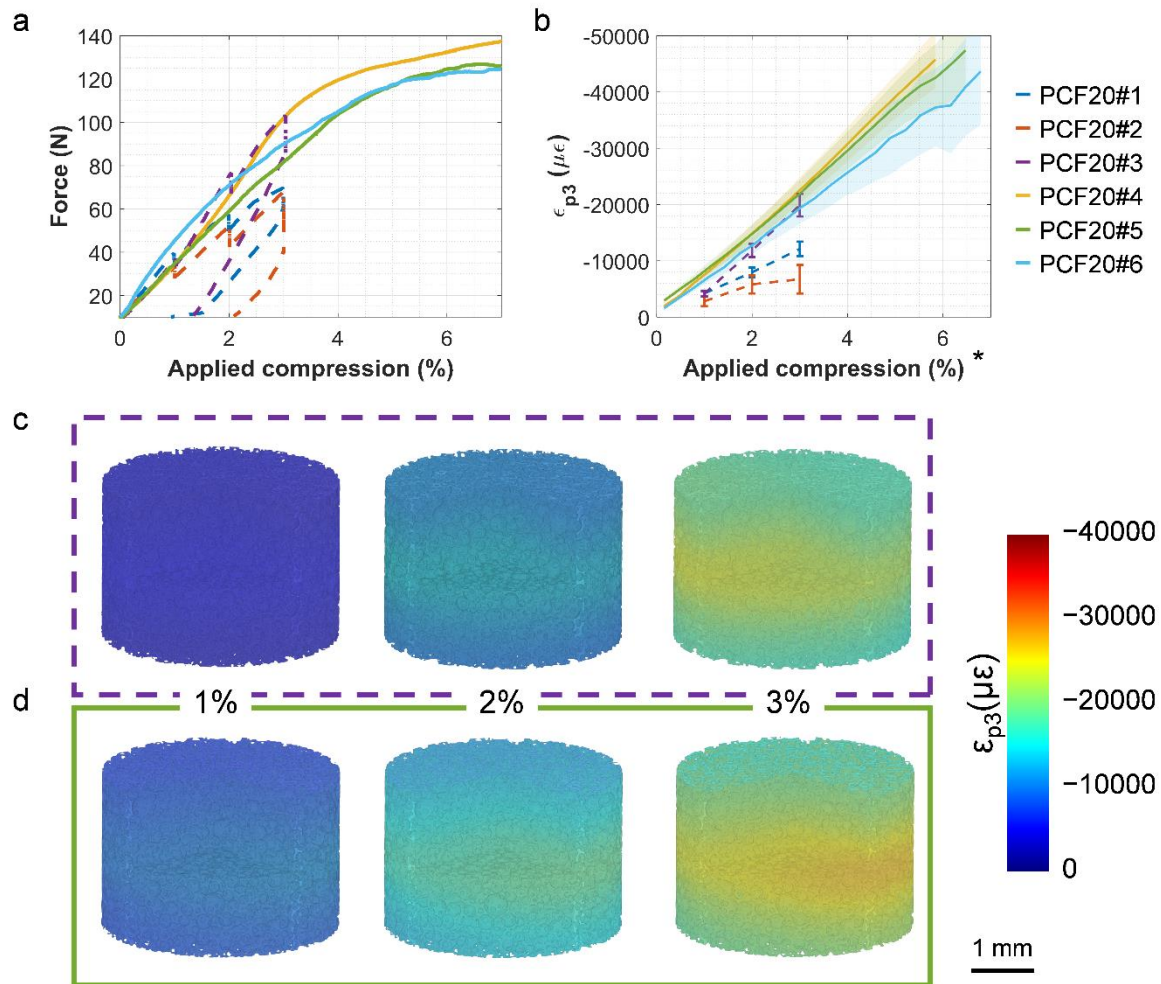
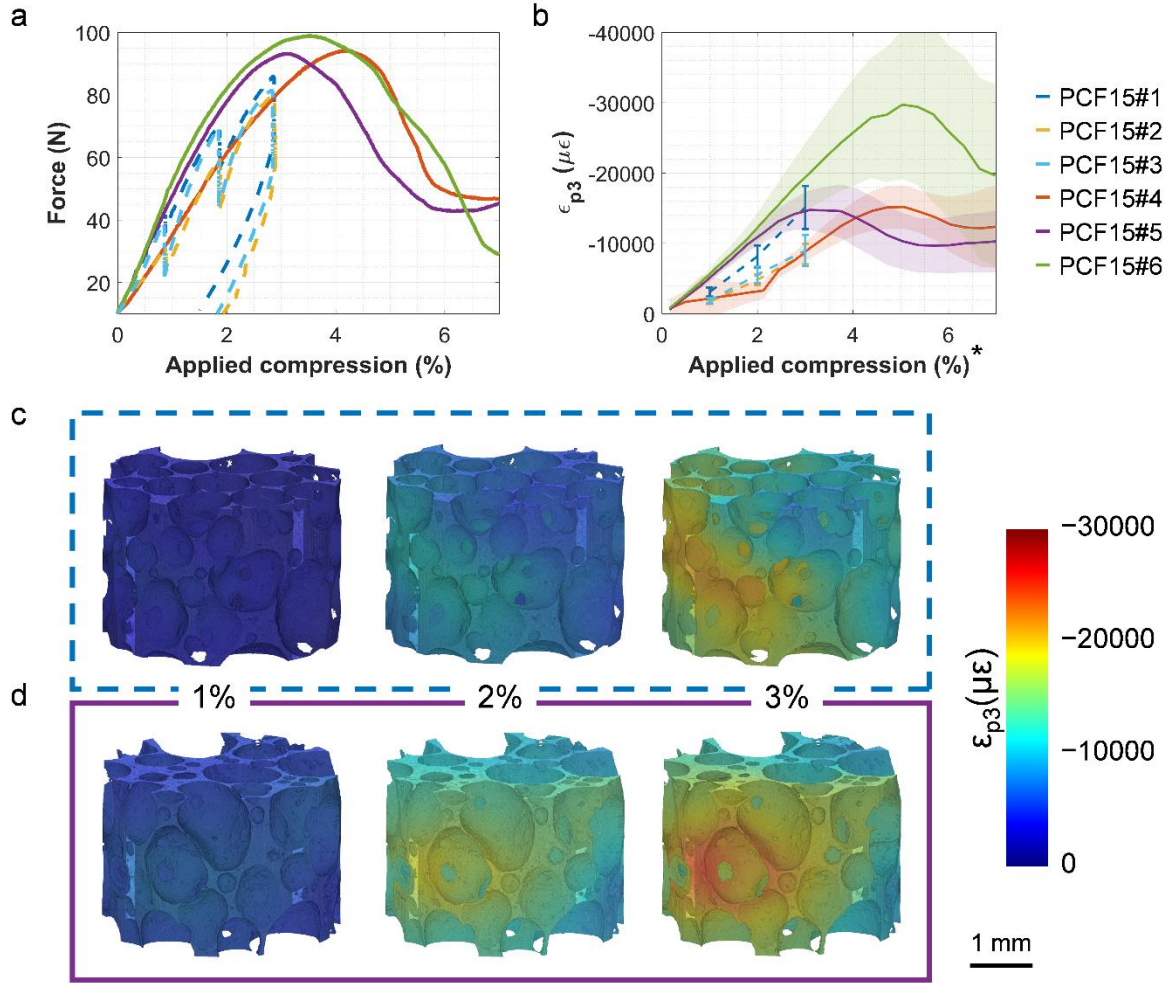


Figure 3. *In situ* SR-microCT compression of PCF20 closed-cell foams subjected to time-lapsed (#1-3) or continuous (#4-6) compression. (a) Force-compression curves for the six specimens. For specimens #1 to #3 the force shows a drop at the end of each compression step, corresponding to the time the specimens were allowed to settle prior to SR-microCT imaging; unloading part of the curve after 3% compression is also shown. (b) DVC-computed minimum principal strains (ϵ_{p3}) at each step (i.e., following each acquired tomogram) in relation to the applied deformation. The solid-dashed lines represent the mean ϵ_{p3} values, with the shaded areas and error bars representing the standard deviation over the entire specimen volume. The 3D full-field third principal strain distribution (ϵ_{p3}) at 1%, 2% and 3% applied compression is visualised for (c) PCF20#3 and (d) PCF20#5 specimens, with specimen-dependent colour-coded bounding boxes as in (a) and (b). The 4D strain distribution for all specimens can be found in Videos S1 and S2. *The applied compression for the specimens imaged dynamically was estimated from the actuator speed, imaging time and delay between each pair of consecutive tomograms.

Cellular open foam specimens (PCF15) displayed a linear monotonic trend up to ~1% compression at apparent level, with yielding occurring between 1.5% to 2% compression

(Figure 4a). The linear elastic behaviour was followed by a significant hardening period (up to 3-4% compression), then by a prolonged softening and strength reduction. Unlike the closed-cell foam, open-cell foams experienced structural failure, which was identified as a drop in the force at apparent level (Figure 4a) and a decrease in the mean local ϵ_{p3} (Figure 4b). The specimens tested dynamically showed higher local ϵ_{p3} levels before yielding compared to those tested in a time-lapsed manner, with the exception of PCF15#4, in which the strain distribution showed higher variation before yielding (Figure 4b, Video S2). The 3D ϵ_{p3} distribution was highly heterogeneous for all specimens, with maximum local strain accumulating in specific regions (Figure 4c, Video S3, S4), which eventually led to local failure in the specimens tested dynamically, followed by a strain redistribution in the structure (Figure 4b, Video S4, **white arrows**). The acquisition of SR-microCT images in a continuous fashion during compression allowed to track the evolution of such local strain accumulation leading to failure at high spatial and temporal resolution, **and it is demonstrated for specimen PCF15#6** (Figure 5). It could be observed how strain built-up around specific thin walls that collapsed when local compressive strains exceeded 30,000 $\mu\epsilon$ (Figure 5, Steps 4-5). Following the first failure and crack development, local strain released from that walls and accumulated in a different region, which also collapsed when for $\epsilon_{p3} < -30,000 \mu\epsilon$ (Figure 5, Steps 5-7).



365 Figure 4. *In situ* SR-microCT compression of PCF15 cellular open foams subjected to time-lapsed (#1-3) or
 366 continuous (#4-6) compression. (a) Force-compression curves for the six specimens. For specimens #1 to #3 the
 367 force shows a drop at the end of each compression step, corresponding to the time the specimens were allowed
 368 to settle prior to SR-microCT imaging; unloading part of the curve after 3% compression is also shown. (b) DVC-
 369 computed minimum principal strains (ϵ_{p3}) at each step (i.e., following each acquired tomogram) in relation to the
 370 applied deformation. The solid-dashed lines represent the mean ϵ_{p3} values, with the shaded areas and error bars
 371 representing the standard deviation over the entire specimen volume. The 3D full-field third principal strain
 372 distribution (ϵ_{p3}) at 1%, 2% and 3% applied compression is visualised for (c) PCF15#1 and (d) PCF15#5 specimens,
 373 with specimen-dependent colour-coded bounding boxes as in (a) and (b). The 4D strain distribution for all
 374 specimens can be found in Videos S3 and S4. *The applied compression for the specimens imaged dynamically
 375 was estimated from the actuator speed, imaging time and delay between each pair of consecutive tomograms.

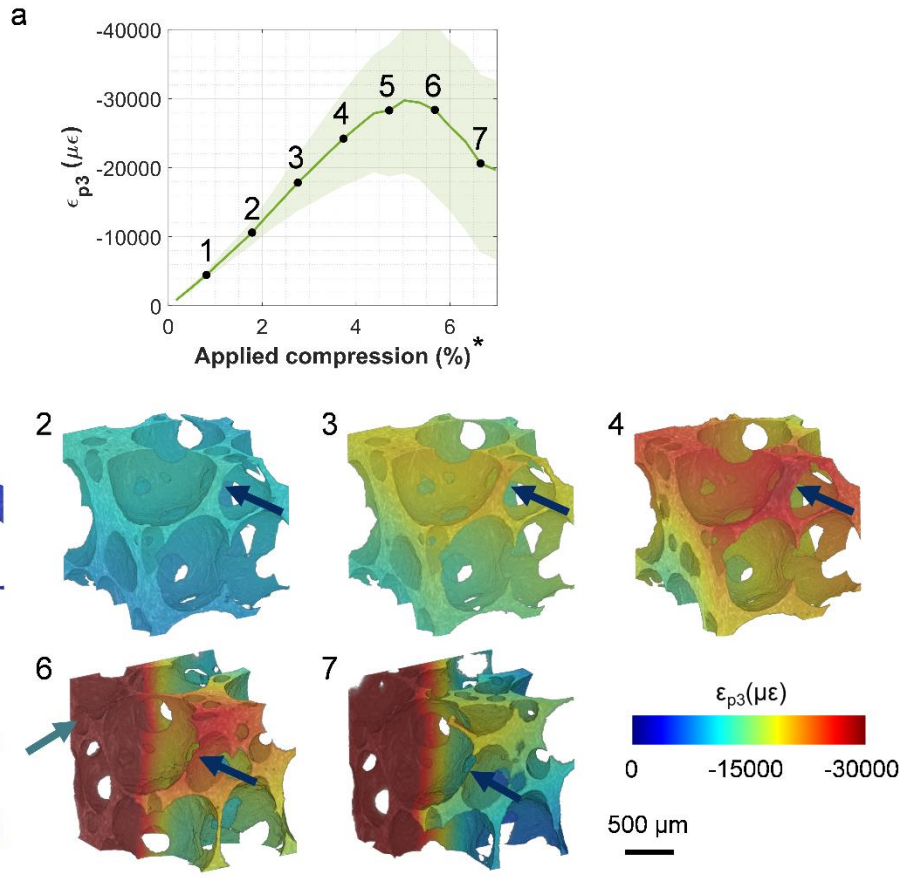


Figure 5. Local failure tracking in a region of interest of PCF15#6. The 3D full-field third principal strain distribution (ϵ_{p3}) at the selected time-points in (a) are represented. Arrows indicate regions of maximum local strains where failure occurred, with blue arrows indicating the first failure event and green arrows the next collapsed regions.

380 Mg-based porous scaffolds displayed a highly similar mechanical behaviour to closed-cell
foams both at apparent and local level (Figure 6) with force-compression curves showing an
elastoplastic response. Initially, scaffolds underwent linear elastic deformation until yielding (~1-
2.5% deformation). As the load increased, a strain hardening region was observed, where the
fibers started to plastically deform and pores to close leading to impingement of the fibers and
consequent densification of the scaffolds (Figure 6). Local ϵ_{p3} increased approximately linear
385 with the applied compression for all specimens, reaching mean values of about -50,000 $\mu\epsilon$ at
10% compression and **an average decrease** of the fibre spacing above 7% (Figure 6b, c);
however, the 4D distribution through the volume evidenced a more homogeneous
compressive deformation in Mg#1 scaffold compared to Mg#2 and Mg#3, which experienced
390 a localised lateral compression (Video S5). Thus, high local ϵ_{p3} values were identified in
regions where fibers were most compressed and collapsed against adjacent ones, where the
spacing between the fibers was reduced (Figure 6d, e).

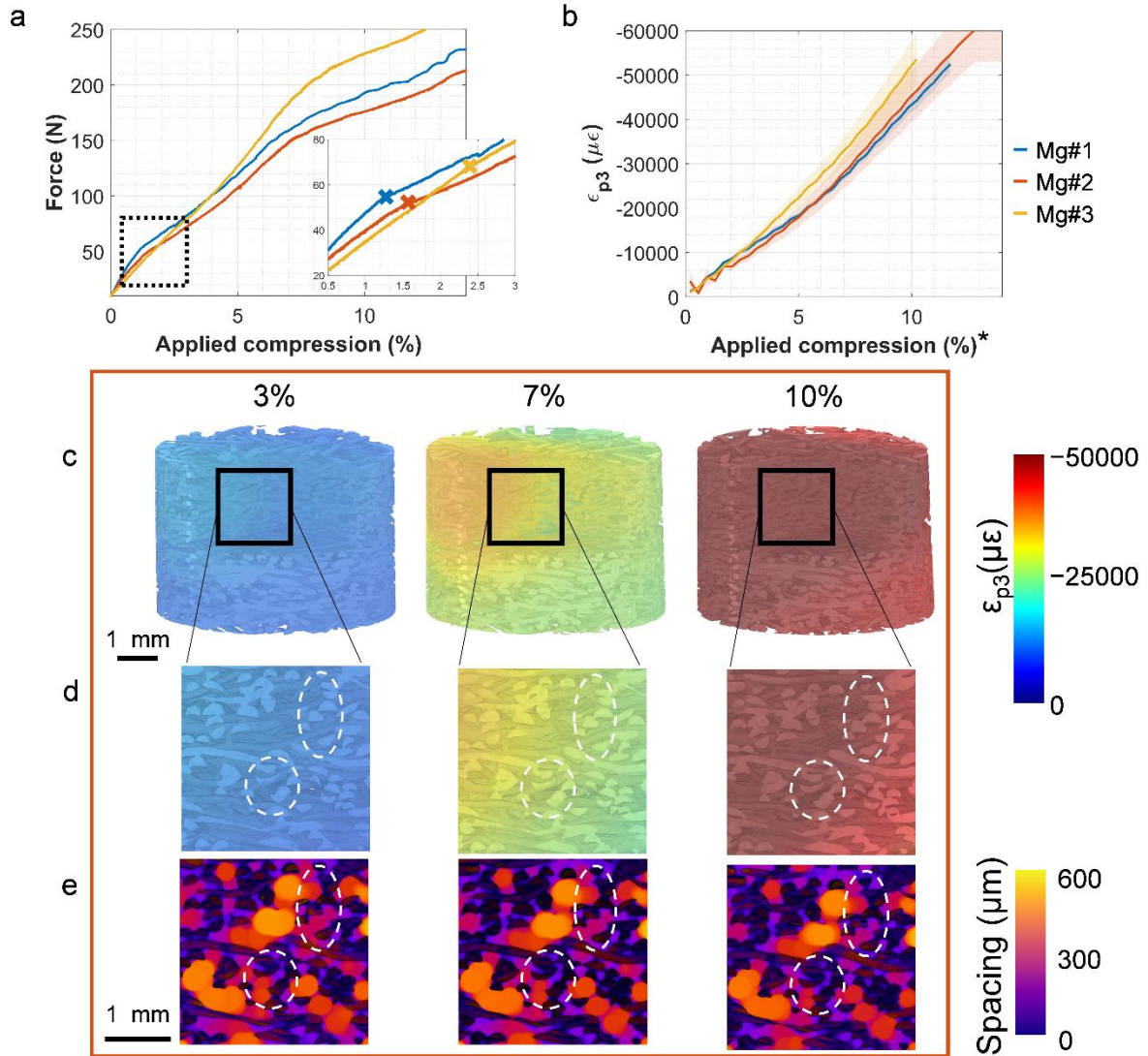


Figure 6. *In situ* SR-microCT compression of Mg-based scaffolds undergoing continuous compression. (a) Force-compression curves for the three specimens. (b) DVC-computed minimum principal strains (ϵ_{p3}) at each step (i.e., following each acquired tomogram) in relation to the applied deformation. The solid lines represent the mean ϵ_{p3} values, with the shaded areas representing the standard deviation over the entire specimen volume. The 3D full-field third principal strain distribution (ϵ_{p3}) at 3%, 7% and 10% compression are visualised for (c) the entire volume of Mg#2 specimen and (d) a magnified region of interest with white area indicating localised impingement of the fibers next to highly strained regions. (e) Colour-coded fibre spacing (i.e., negative space of the fibres) in the same region of interest of (d) with white ovals indicating pores closing. The 4D strain distribution for all specimens can be found in Video S5. *The applied compression was estimated from the actuator speed, imaging time and delay between each pair of consecutive tomograms.

The high heterogeneity in the microstructure of trabecular bone specimens led to a more variable mechanical behaviour under compression compared to the above reported synthetic materials (Figure 7). At an apparent level, force-compression curves showed an initial toe region due to the imperfections on the initial co-planarity of the two endcaps. Thereafter, all the specimens showed a monotonic trend that was linear until failure (Figure 7a). The ultimate

load correlated well with the bone volume fraction ($R^2 = 0.73$), with plate-like structures (TB#1 and TB#2) taking higher load before failure compared to rod-like structures (TB#3 and TB#4) and the mixed configuration of TB#5 specimen (Figure 7a, Video S6). Similarly, mean local ϵ_{p3} showed an increasing linear trend with the applied compression prior to failure, after which strains built-up more steeply due to the accumulation of cracks in the trabecular structure (Figure 7b, Video S6). Before cracks appeared, mean local ϵ_{p3} ranged between $-10,000 \mu\epsilon$ to $-15,000 \mu\epsilon$ (Figure 7b), however, the strain distribution was highly heterogeneous throughout the volume, with localised regions exceeding those values (Figure 7c, d). The 4D evaluation of the strain distribution demonstrated that maximum strain levels accumulated in regions where failure, in the form of cracks, later occurred (Figure 7c, d, Video S6). Additionally, the rod-like trabecular structure seemed to be able to sustain higher compressive strains before fracture (Figure 7c) compared to the plate-like structure (Figure 7d).

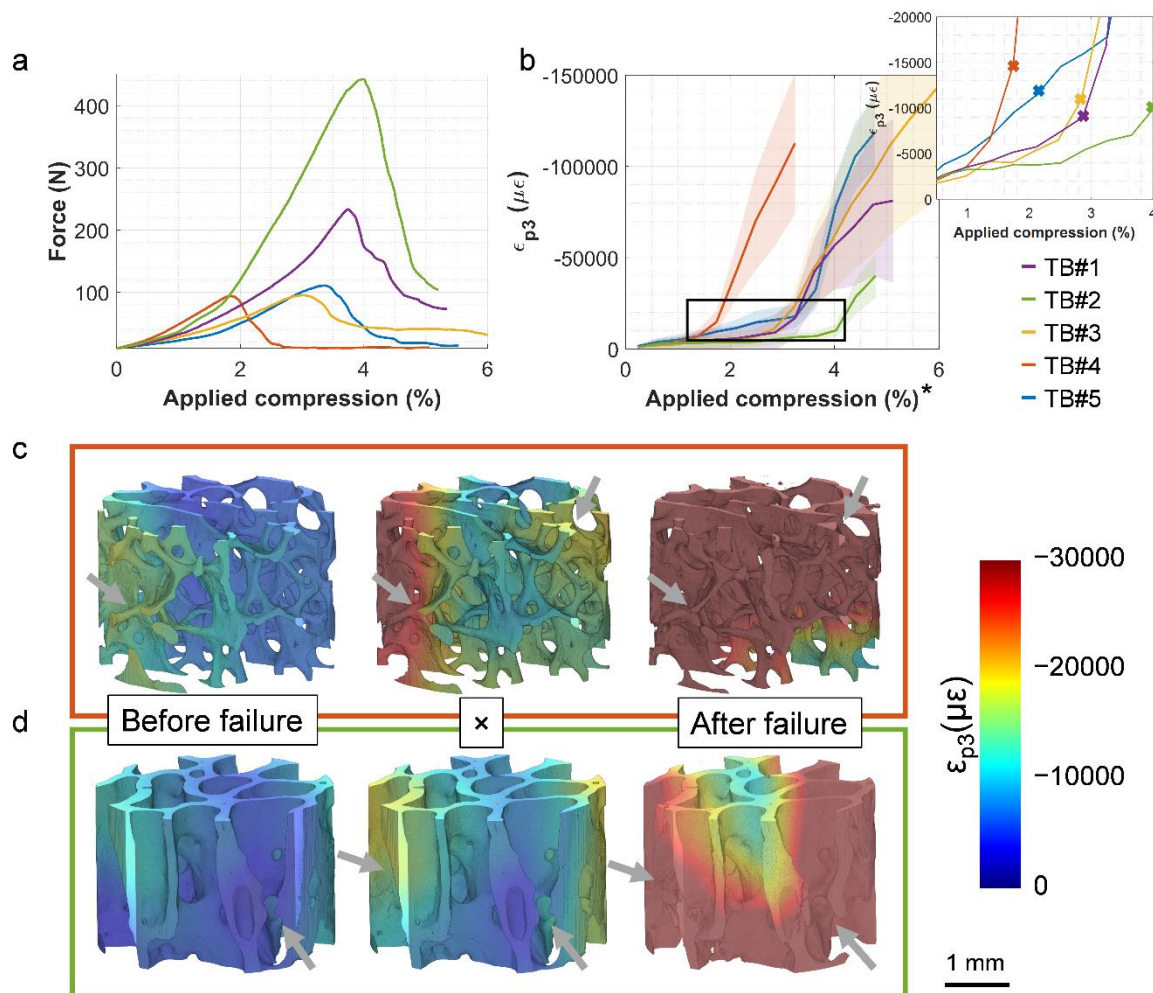


Figure 7. *In situ* SR-microCT compression of trabecular bone (TB) structures undergoing continuous compression. (a) Force-compression curves for the five tested specimens. (b) DVC-computed minimum principal strains (ϵ_{p3}) at each step (i.e., following each acquired tomogram) in relation to the applied deformation. The solid lines represent the mean ϵ_{p3} values, with the shaded areas representing the standard deviation over the entire specimen volume.

1 × symbols in the insert indicate step prior to cracking. The 3D full-field third principal strain distribution (ϵ_{p3}) before,
2 during and after failure is visualised for (c) TB#4 (rod-like structure) and (d) TB#2 (plate-like structure) specimens,
3 with specimen-dependent colour-coded bounding boxes as in (a) and (b). Arrows indicate highly strained regions
4 tracked over time where cracks in the structure appeared. The 4D strain distribution for all specimens can be found
5 430 in Video S6. *The applied compression was estimated from the actuator speed, imaging time and delay between
6 each pair of consecutive tomograms.
7

8
9 Similar to trabecular bone, the mechanical behaviour of cortical bone showed noticeable intra-
10 specimen differences (Figure 8). All specimens also displayed an initial toe region in the force-
11 compression curves, followed by a monotonic linear trend up to failure (Figure 8a). Unlike
12 trabecular bone, the differences in the apparent mechanical behaviour, both stiffness and load
13 435 to failure, were not related to the microstructure but rather to the off-axis compression and
14 consequent tilting of specimens CB#1 and CB#3 during compression (Video S7). Prior to
15 failure, mean local ϵ_{p3} showed a mostly uniform distribution with a linear increase (Figure 8b).
16 Additionally, local strains accumulated in regions where longitudinal cracks, piercing the entire
17 cortical volume, were observed after failure (Figure 8c, d). Such strains did not exceed
18 440 $-10,000 \mu\epsilon$ locally before crack development, with mean local ϵ_{p3} in the analysed volume
19 ranging between $-4,119 \mu\epsilon$ and $-7,273 \mu\epsilon$ among the four specimens (Figure 8b, Video S7).
20
21
22
23
24
25
26
27
28
29
30
31
32
33
34
35
36
37
38
39
40
41
42
43
44
45
46
47
48
49
50
51
52
53
54
55
56
57
58
59
60
61
62
63
64
65

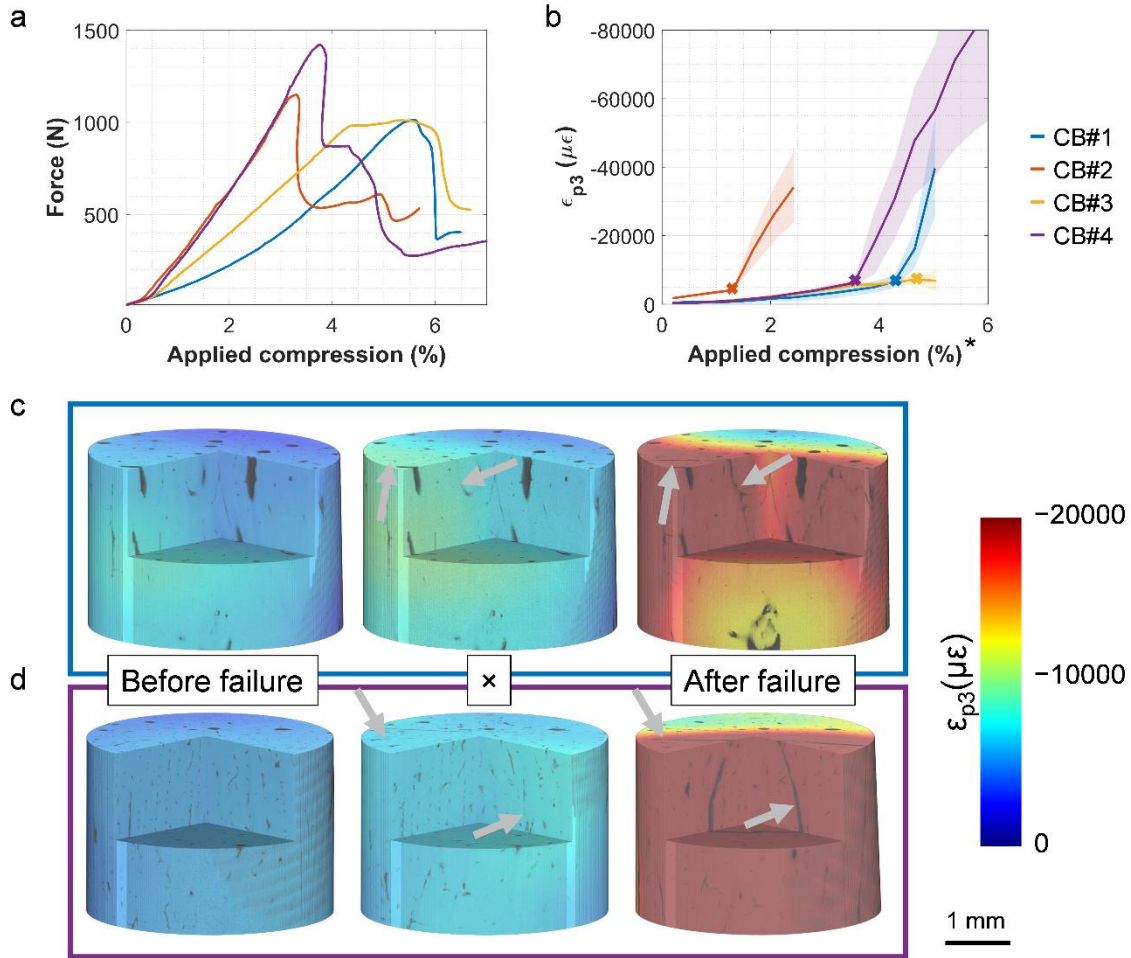
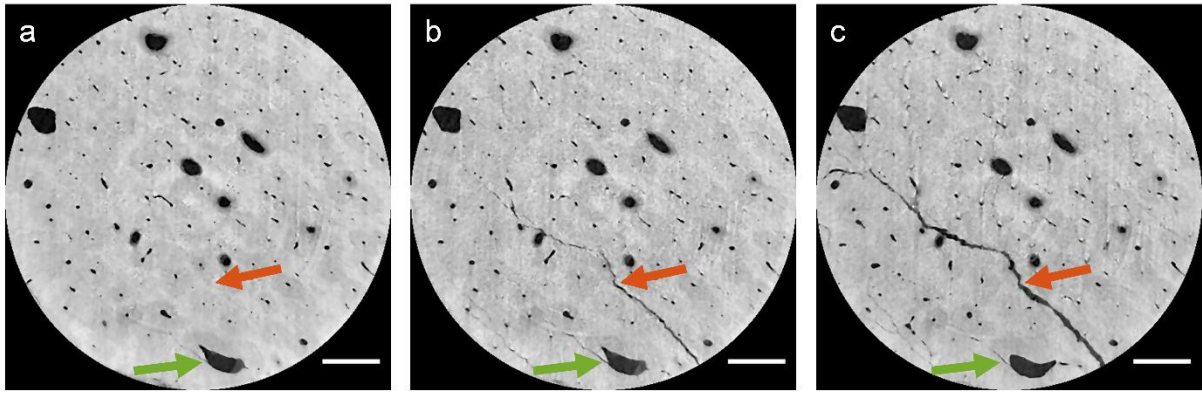


Figure 8. *In situ* SR-microCT compression of cortical bone (CB) structures undergoing continuous compression. (a) Force-compression curves for the four tested specimens. (b) DVC-computed minimum principal strains (ϵ_{p3}) at each step (i.e., following each acquired tomogram) in relation to the applied deformation. The solid lines represent the mean ϵ_{p3} values, with the shaded areas representing the standard deviation over the entire specimen volume. \times symbols in the insert indicate step prior to cracking. The 3D full-field third principal strain distribution (ϵ_{p3}) before, during and after failure is visualised for (c) CB#1 and (d) CB#4 specimens, with specimen-dependent colour-coded bounding boxes as in (a) and (b). Arrows indicate highly strained regions tracked over time where cracks in the structure appeared. The 4D strain distribution for all specimens can be found in Video S7. *The applied compression was estimated from the actuator speed, imaging time and delay between each pair of consecutive tomograms.

Some cracks were found to initiate next to the Harversian canals and propagated through the structure by deviating among some osteons (Figure 9). The development of cracks in the specimens resulted in a more heterogeneous strain distribution and a sudden increase in local ϵ_{p3} , with maximum strain values around the crack region exceeding $-20,000 \mu\epsilon$ (Figure 8b, Video S7).



460 **Figure 9. Crack initiation and propagation in CB#5 cortical bone specimen. (a) Some cracks initiated next to a**
 465 **Haversian canal (green arrow), in the more strained regions (Figure 8c). (b, c) Larger cracks promoting structural**
 470 **failure as a result of strain heterogeneity (Fig. 8d) showed a deviation among the osteons during propagation**
 475 **(orange arrow). Scale bars: 500 μm .**

Force-compression curves for the cuttlebone specimen showed an initial linear region up to
 465 ~6% compression; then, yielding occurred and the pillars at the bottom started to collapse,
 which resulted in a drop in the force. Thereafter, a plateau was observed while the pillars were
 compressed followed by a second linear increase in the force up to ~18% compression, where
 a second layer of pillars failed and thus, the force dropped (Figure 10a). The full-field ϵ_{p3}
 470 distribution was highly heterogeneous in the analysed volume, with mean strains showing an
 irregular increasing trend (Figure 10b). Local ϵ_{p3} concentrations were found around the septa,
 which then transferred the load through the pillars (Figure 10c), leading to an intermittent strain
 accumulation when followed in 4D (Video S8). While the septa were able to withstand local
 compressive strains below -10,000 $\mu\epsilon$ without collapsing, the pillars seemed to fail at
 approximately -8,000 $\mu\epsilon$, and maximum local ϵ_{p3} were then observed in the fracture region
 475 (Figure 9c).

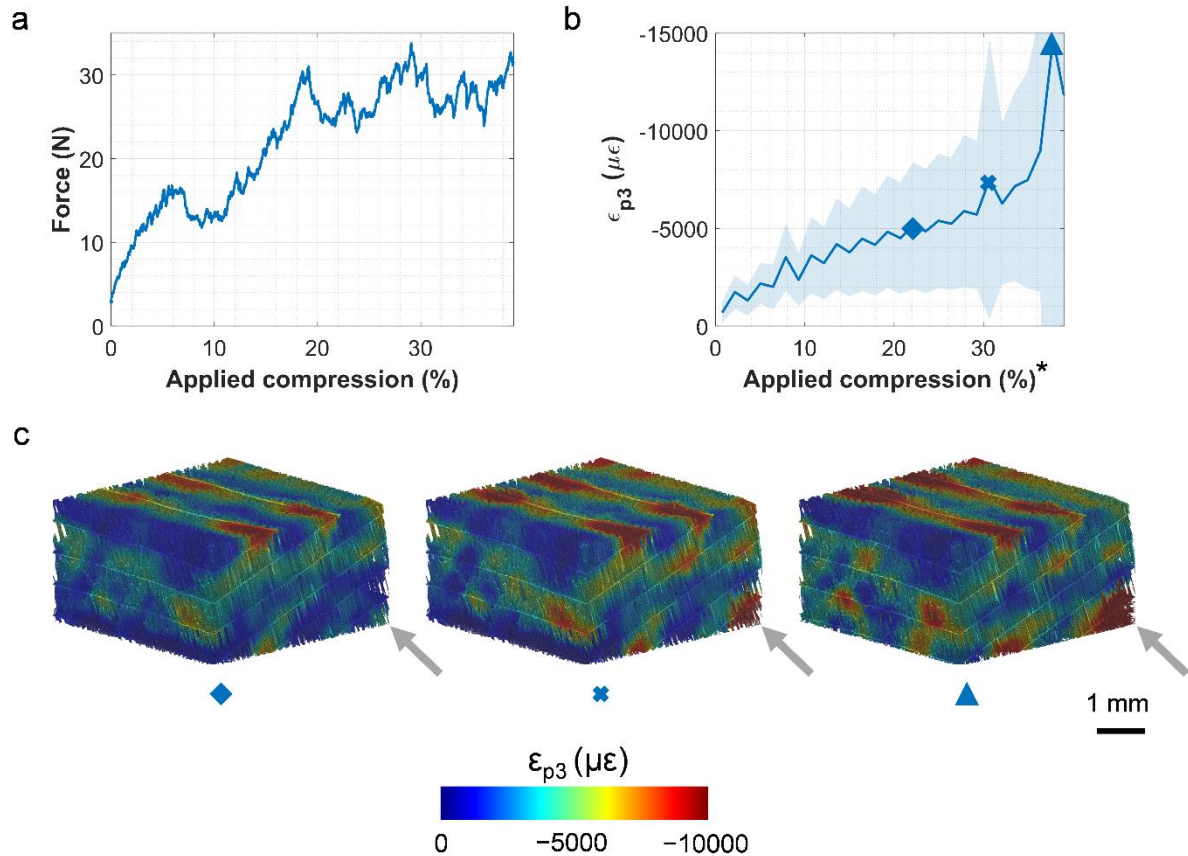


Figure 10. *In situ* SR-microCT compression of cuttlebone (CF) structure undergoing continuous compression. (a) Force-compression curves for the tested specimen. (b) DVC-computed minimum principal strains (ϵ_{p3}) at each step (i.e., following each acquired tomogram) in relation to the applied deformation. The solid lines represent the mean ϵ_{p3} values, with the shaded areas representing the standard deviation over the entire specimen volume. (c) The 3D full-field third principal strain distribution (ϵ_{p3}) at the compression levels denoted by the symbols. Arrows indicate highly strained regions tracked in the pillars over time where collapse was observed. The 4D strain distribution can be found in Video S8. *The applied compression was estimated from the actuator speed, imaging time and delay between each pair of consecutive tomograms.

4. Discussion

In this study, the four-dimensional (4D) deformation behaviour of biological and synthetic porous materials was investigated via *in situ* time-resolved synchrotron micro-computed tomography (SR-microCT) with uniaxial compression and digital volume correlation (DVC). **Time-resolved** tomographic imaging of the compressive deformation allowed the identification of damage initiation and progression, as well as the quantification of the full-field strain distribution and evolution in various biostructures, circumventing the characteristic stress-relaxation effects of porous viscoelastic materials subjected to time-lapsed mechanical testing.

The investigated porous materials herein presented included a wide range of microstructural features, thus allowing the assessment of the method for different material porosities, wall

495 thicknesses and pore sizes. The imaging settings were fine-tuned for each biostructure in
1 order to minimise blurring and imaging artefacts during continuous deformation that could
2 affect DVC computation. Features thinner than 50 μm , such as cuttlebone pillars and cortical
3 bone canals (Figure 2, Table 3), were resolved both in static and dynamic conditions with high
4 **nominal** (i.e., 5.6 to 10.4 μm **effective** voxel size) and temporal (i.e., 12 to 22.2 s per scan)
5 resolution. All specimens were compressed at a displacement rate of 1.67 $\mu\text{m s}^{-1}$ except the
6 cuttlebone which used 3.33 $\mu\text{m s}^{-1}$, resulting in a total compression of 22 to 40 μm (i.e., 3 to 7
7 times the voxel size) per scan. Such a ratio of total compression over voxel size is in line with
8 previous work on the semi-solid deformation of granular alloys using time-resolved *in situ* SR-
9 microCT mechanics [51,52,54]. However, a qualitative and semi-quantitative comparison of
10 the contrast and definition of the main features of interest in statically vs dynamically acquired
11 images have not been previously reported. In this study, it was shown that the compression
12 applied did not compromise image quality throughout the mechanical tests and only some
13 blurring and distortion was observed in regions of structural failure (Figure 2) as such
14 phenomena, particularly in the propagation stage, occur due to cracks developing at a faster
15 rate than concomitant image acquisition.
16
17
18
19
20
21
22
23
24
25 510

A comparison between time-lapsed and continuous stress-strain curves has previously been
26 assessed in aluminium foams and trabecular bone cylinders subjected to *in situ* microCT
27 compression [32], showing no significant differences between the curves. However, to the
28 authors' knowledge, comparison of time-lapsed versus continuous DVC-computed local
29 strains has not been previously studied. Here, synthetic foams of different porosities were
30 used to assess such differences due to their anisotropic and inhomogeneous nature, very
31 similar to that of trabecular bone, but with highly reproducible microarchitecture and overall
32 consistency in mechanical behaviour (Table 2). Similar to previous studies, the elastic part of
33 the time-lapsed and continuous force-compression curves showed almost identical shapes,
34 with a trend towards lower forces close to the yielding point in the time-lapsed test (Figure 3a,
35 4a). As a 10-min waiting period was imposed at the end of the application of each strain step
36 in the time-lapsed compression test, the stress relaxation reached a plateau. This inherent
37 relaxation was responsible for the lower measured forces in the yielding phase of the curve
38 and in a local strain redistribution between steps (Figures 3, 4). As such, the full-field strain
39 analysis of both time-lapsed and continuous test showed a comparable 3D distribution, yet
40 lower strain magnitudes were observed in the time-lapsed test (Figures 3c, 4c). This was more
41 important in the closed-cell foams PCF20, where local compressive strains following stress-
42 relaxation were up to three-fold lower than during compression (Figure 3b). These results
43 highlight the need for fast imaging during *in situ* microCT mechanical testing to capture the
44
45
46
47
48
49
50
51 525

1
2
3
4
5
6
7
8
9
10
11
12
13
14
15
16
17
18
19
20
21
22
23
24
25
26
27
28
29
30
31
32
33
34
35
36
37
38
39
40
41
42
43
44
45
46
47
48
49
50
51
52
53
54
55
56
57
58
59
60
61
62
63
64
65

530 dynamic deformation behaviour of porous synthetic and biological materials, allowing to fully appreciate the strain-damage relationships.

Despite the porous nature of all the studied materials, the higher solid volume fraction and density of cortical bone specimens resulted in a more brittle failure when loaded in compression. On the other hand, the remaining biostructures, including synthetic

535 biostructures, trabecular bone and cuttlebone, deformed by the elastic bending and buckling as well as the plastic collapse of their struts/walls when loaded. Both closed-cell PCF20 and open-porous Mg foams showed a ductile behaviour and the plastic deformation of their struts/fibers and closing of their pores in highly strained regions, resulting in a densification of the structure, which was more pronounced towards its centre due to the applied uniaxial compression (Figure 3c, 6c). On the other hand, the open cellular foam PCF15 and trabecular bone specimens displayed a more heterogeneous strain distribution, due to the elastic bending and buckling of the struts and trabeculae (Fig 4c, 7c, d). As such, strain accumulation was observed in specific walls and trabeculae undergoing higher deformation due to bending and buckling, which ultimately resulted in fracture and overall failure of the structure.

540 Moreover, the acquisition of multiple microCT scans through the compression test also allowed to track the failure initiation and progression with high spatial and temporal resolution (Figure 5). While the accumulation of compressive strains led to fracture of the walls/trabeculae, overloading the structures beyond the primary failure point resulted in a strain release of the failed region coordinated with a strain build-up in another region (videos S4, S6). This strain release behaviour following failure in the form of cracks has been previously observed in trabecular bone and bone-biomaterial systems during time-lapsed *in situ* microCT compression [30], where the formation of microcracks caused the redistribution of compressive strains in the structure and an increase of tensile and shear strains in the failed regions. Interestingly, local compressive strains in the cuttlebone specimen displayed a

555 continuous redistribution through the mechanical test in non-fractured regions, due to its distinctive microstructure, where the stiff and hard layers within the septa alternate with more compliant and ductile zones, possibly to direct failure to internal 'sacrificial' structures via chamber collapse, maintaining overall integrity and function of the cuttlebone as a buoyancy regulator [77]. Therefore, the septa bore higher compressive strains without structural failure, that were transferred to the different layers through the pillars (Video S8). More cuttlebone specimens will need to be tested in future studies to further understand the load and strain transfer ability of such a complex biostructure. Nevertheless, these preliminary results demonstrate the ability of the method to capture the time-resolved deformation of the thin pillars and septa of cuttlebone material.

565 DVC based on *in situ* time-lapsed mechanical testing with microCT is increasingly gaining
1 interest to quantify the 3D deformation mechanisms of bone at different length scales, from
2 organ to tissue level [25,78]. Most studies focused on trabecular bone at the macro- [78] and
3 mesoscale [30,79] due to its intrinsic microarchitecture, which provides a natural greyscale
4 pattern for the DVC method [80]. However, the higher-spatial resolution achieved using SR-
5 microCT have enabled the assessment of trabecular bone strains at tissue level and
6 consequently, its relation to microdamage initiation and progression [57,58,81]. Despite the
7 high-resolution images acquired in this study, with a nominal resolution of 6.5 μm , the coarse
8 subvolumes used for the DVC analysis (i.e., 312 μm), did not allow to obtain strain
9 measurements at tissue level but at the whole trabecular thickness level so to minimise the
10 uncertainties of the method [24,82]. The continuous full-field strain analysis herein presented
11 show similar strain patterns to those previously reported at a higher resolution using time-
12 lapsed testing, but approximately two-fold increased strain magnitudes both before and after
13 failure [81]. Interestingly, the mean DVC-computed strains following yielding but prior to failure
14 ranged between $-10,000 \mu\epsilon$ to $-15,000 \mu\epsilon$ (Fig. 7b), which is in line with previously reported
15 yielding strain values for human trabecular bone in compression ($\sim -10,000 \mu\epsilon$ [83,84]).
16 Recently, Turunen et al. [85] reported sub-trabecular strain measurements using time-lapsed
17 *in situ* high-resolution (i.e. 3.6 μm voxel size) SR-microCT mechanics, where subvolumes as
18 small as 10 voxels were employed for the DVC analysis, resulting in a highly heterogeneous
19 strain distribution within the trabecular bone tissue, and average volumetric strains up to
20 77,000 $\mu\epsilon$ at the global yield point, prior to fracture, one order of magnitude higher than those
21 in this study. However, large DVC strain uncertainties were reported (MAER above 1500 $\mu\epsilon$),
22 thus it still remains unclear whether such strain measurements may be largely influenced by
23 noise, as few features (i.e. osteocyte lacunae) may be found within that subvolume size in
24 trabecular bone tissue [86] to allow an accurate DVC computation.

580 To date, only few studies have been carried out for cortical bone specimens using *in situ*
585 microCT mechanics and DVC [55,87,88], with the present one being the first evaluating
cortical tissue mechanics in a continuous fashion. Nevertheless, the measured local average
590 strain of $\sim -6,000 \mu\epsilon$ in cortical bone specimens following yielding prior to failure is well aligned
to those previously reported from traditional uniaxial compression, which ranged from $-6,600$
595 $\mu\epsilon$ to $-10,700 \mu\epsilon$ in the axial direction of human cortical bone [89]. Moreover, the tissue-
averaged local strains here presented showed a similar pattern to those measured using high-
speed optical imaging and digital image correlation [90], where the strain distribution prior to
yielding was approximately constant (i.e. homogeneous distribution) and small but broadened
significantly after it, indicating the onset of high strain regions locally (Figure 8b), that led to
600 failure (Video S7). Peña Fernández et al. [55] recently showed the dynamic strain evolution in

1 cortical bone specimens that had previously been subjected to cyclic loading using the same
2 methodology here reported. Similar to the less cycled specimens therein reported, the
3 specimens used in this study displayed a structural collapse due to the presence of a main
4 longitudinal crack piercing the bone volume longitudinally (Video S7) but higher strains prior
5 to failure, which may be related to some damage already occurring during cyclic loading in
6 [55].
7

8
9
10 The ability of DVC to provide local strain measurements in relation to bone microstructure
11 allowed to identify higher compressive strains in trabecular rods compared to trabecular plates
12 prior to failure (Video S6), suggesting the ability of rod-like trabecular structure to sustain
13 higher deformation without causing a catastrophic failure of the structure. Liu et al. [91]
14 conducted a nonlinear micro-finite element (FE) analysis to evaluate the role of trabecular
15 types (i.e. plates and rods) in the failure initiation and progression for human vertebral
16 trabecular bone. It was shown that more trabecular rods failed (i.e., reached tissue strain
17 yielding values) at the initiation of compression while more plates failed around the apparent
18 yielding point, suggesting that local failure initiated primarily at trabecular rods. The high
19 temporal and spatial resolution employed in this study allowed to observe that despite the
20 higher strains sustained by trabecular rods, above tissue yielding values, failure in the form of
21 fracture occurred at higher strain magnitudes (Figure 7c), whereas plate-like structures failed
22 at lower strain levels (Figure 7d). These results evidenced the relationships between structure
23 and function in bone tissue, and the importance of local strain measurements to describe and
24 assess the elastic instabilities of bone structure that cannot be entirely described by the
25 material properties of the tissue. However, such relationships were difficult to observe in
26 cortical bone specimens, mainly due to the coarse DVC-resolution (~300 µm), approximately
27 double than the diameter of the osteons in bovine femur [92]. Osteons are complex
28 mechanical features that can act both as stress concentrators, where cracks may initiate
29 (Figure 9a), or as crack propagation barriers (Figure 9b, c). Here, it was observed that some
30 cracks initiated in regions highly strained (Figure 8c, d) and others developed as a result of an
31 overall structural strain heterogeneity. However, osteon-level strain measurements remain
32 missing and higher-resolution imaging would be needed to provide tissue-level strains [55,87],
33 able to better elucidate the associations between osteons deformation and damage initiation
34 and propagation. Therefore, further improvement of the experimental technique herein
35 presented, mainly imaging and DVC spatial resolution, would be needed to fully characterise
36 the links of bone microstructural features (i.e., trabecular rods and plates, osteons) and local
37 strains leading to the initiation of local failure in bone tissue.
38
39
40
41
42
43
44
45
46
47
48
49
50
51
52
53
54
55
56

57
58 Unfortunately, it is known that high exposures to SR X-ray radiation lead to a loss of
59 mechanical and structural integrity of bone as a result of collagen matrix degradation [93,94];
60
61
62
63
64
65

1 therefore, the radiation dose absorbed by the specimens needs to be considered when
2 performing *in situ* SR-microCT mechanical tests. Here, the experimental session at Diamond
3 Light Source (I13-2) was planned to ensure that specific environmental and technical aspects
4 (e.g., loading stage, filters) were in line to those of previous work from the authors [57,58],
5 640 from which the radiation doses were estimated, resulting in 34.81 Gy/s and 45.27 Gy/s for
6 cortical and trabecular bone specimens, respectively. Thus, the total radiation dose was below
7 20.1 kGy during the continuous testing in the present study (Table S2) and far below the
8 currently define 'safe' threshold of 35 kGy [94]); hence, minimising irradiation-induced damage
9 [58,94]. Nevertheless, it must be noted that the dose estimation considered bone specimens
10 as homogeneous cylinders with a specific apparent density, which may underestimate local
11 dose deposition and consequent damage, particularly in trabecular bone specimens.
12 Specimen-dependent dose simulation may provide further insight on the effect of SR X-ray
13 645 radiation on the mechanical weakening of bone; however, this was beyond the aims of this
14 study. Further investigations are, therefore, encouraged to better understand the mechanisms
15 leading to collagen degradation and how the X-ray beam-induced thermal gradients [88]
16 contribute to the tissue deterioration. Likewise, the radiation dose absorbed by the cuttlebone
17 specimen could not be estimated due to a lack of data (i.e., energy and flux). Similar to
18 collagen in bone, β -chitin, the main protein in the organic matrix of cuttlebone, is very sensitive
19 to radiation damage [95]. However, the organic matter in cuttlebone is much lower than in
20 bone (~ 4% in cuttlebone, 30% in bone), so the radiation dose needed to deteriorate cuttlebone
21 650 integrity may be higher than for bone and it is therefore within reason to assume the tissue did
22 not undergo any significant denaturation. This also remains object of future experiments
23 aiming to fully characterise the mechanical behaviour of cuttlebone.

24
25
26
27
28
29
30 655
31
32
33
34
35
36
37
38
39 660 The study of the time-dependent viscoelastic deformation of bone is of great clinical interest
40 to better understand non-traumatic-fractures due to prolonged load over time, loosening of
41 orthopaedic implants due to cyclic loads or the energy absorption and dissipation ability of
42 bone during dynamic loading [96–99]. As such, creep and stress relaxation tests have been
43 previously used to characterise the viscoelasticity of bone [34]. However, it is also known that
44 665 the mechanical response of bone highly depends on its microarchitecture. Therefore, some
45 studies have developed microFE models of bone accounting for the viscoelasticity of the tissue
46 and validated against creep and stress relaxation experiments [38,100]. However, a validation
47 of local measurements remains missing due to the lack of 3D experimental data. In that
48 perspective, the results herein presented would be highly beneficial to inform, refine and
49 validate such models. Moreover, the combination of continuous *in situ* SR-microCT mechanics
50 and DVC will allow to quantify the local deformation causing both creep and stress relaxation.
51 In this context, Haug et al. [49] recently showed the DVC-computed local displacements and
52
53
54
55
56 670
57
58
59
60
61
62
63
64
65

1
2
3 675 **their** evolution over time of agglomerates during stress relaxation of vaterite compacts imaged
4 at high temporal (i.e. 18 s) and spatial (0.1625 μm voxel size) resolution using SR light. Such
5 experimental technique and results are therefore encouraging in **the** field of biomechanics to
6 better understand the time-dependent mechanical behaviour of bone and biomaterials. As
7 such, further optimisation of both imaging acquisition and reconstruction algorithms [41] are
8 needed to enable the mechanical reproduction of relevant physiological strain rates [101] to
9 fully characterise the viscoelasticity and micromechanics of biomaterials and consequently, to
10 extend the technique to softer biological tissues displaying higher viscoelasticity [26,27].
11 680

14 5. Conclusion

16 Time-resolved *in situ* SR-microCT mechanics and DVC were used to achieve unprecedented
17 qualitative and quantitative analysis of the compressive deformation for bone and bone
18 analogues. The results showed how continuous mechanical testing allowed the dynamic
19 deformation of porous viscoelastic materials to be characterised, enhancing and
20 complementing the information obtained from traditional time-lapsed testing. High-speed SR-
21 685 microCT imaging was essential to elucidate the relationship between local strains and both
22 damage initiation and propagation during uniaxial compression of biostructures undergoing
23 plastic deformation, bending and/or buckling of their main microstructural elements. The
24 findings of this article highlight the importance of *in situ* SR-microCT dynamic experiments for
25 characterising the time-dependent mechanical behaviour of biomaterials. This has the
26 potential to better inform the effects of clinical conditions on the biomechanical responses of
27 biological tissues.
28
29 690

37 Acknowledgments

39 695 The authors gratefully acknowledge Christoph Rau and Shashidhara Marathe for support
40 during the experimental sessions at the Diamond-Manchester Imaging Branchline I13-2 of
41 Diamond Light Source (UK), under proposals MG22575 and MT20132. We further
42 acknowledge the Zeiss Global Centre (University of Portsmouth, UK) for providing imaging
43 analysis facilities. H.A. was supported by The Royal Society, IEC\R3\170065. This work was
44 supported by Biotrics Biomaterials AG (Germany).
45
46 700

50 Conflict of interest statement

52 F.W. is an employee of Biotrics Bioimplants AG which partially funded this study. The
53 remaining authors declare that they have no known conflict of interests.
54
55
56
57
58
59
60
61
62
63
64
65

Data availability statement

Raw data were generated at Diamond Light Source, I13-2 beamline. Derived data supporting the findings of this study are available on request from the corresponding author, M.P.F.

References

- [1] J.Y. Rho, L. Kuhn-Spearing, P. Zioupos, Mechanical properties and the hierarchical structure of bone, *Med. Eng. Phys.* 20 (1998) 92–102. [https://doi.org/10.1016/S1350-4533\(98\)00007-1](https://doi.org/10.1016/S1350-4533(98)00007-1).
- [2] P. Datta, V. Vyas, S. Dhara, A.R. Chowdhury, A. Barui, Anisotropy Properties of Tissues: A Basis for Fabrication of Biomimetic Anisotropic Scaffolds for Tissue Engineering, *J. Bionic Eng.* 16 (2019) 842–868. <https://doi.org/10.1007/s42235-019-0101-9>.
- [3] L. Edgar, K. McNamara, T. Wong, R. Tamburrini, R. Katari, G. Orlando, Heterogeneity of Scaffold Biomaterials in Tissue Engineering, *Materials (Basel)*. 9 (2016) 332. <https://doi.org/10.3390/ma9050332>.
- [4] K. Bobe, E. Willbold, I. Morgenthal, O. Andersen, T. Studnitzky, J. Nellesen, W. Tillmann, C. Vogt, K. Vano, F. Witte, In vitro and in vivo evaluation of biodegradable, open-porous scaffolds made of sintered magnesium W4 short fibres, *Acta Biomater.* 9 (2013) 8611–8623. <https://doi.org/10.1016/j.actbio.2013.03.035>.
- [5] S. Gómez, M.D. Vlad, J. López, M. Navarro, E. Fernández, Characterization and three-dimensional reconstruction of synthetic bone model foams, *Mater. Sci. Eng. C.* 33 (2013) 3329–3335. <https://doi.org/10.1016/j.msec.2013.04.013>.
- [6] S. Bailey, D. Vashishth, Mechanical Characterization of Bone: State of the Art in Experimental Approaches—What Types of Experiments Do People Do and How Does One Interpret the Results?, *Curr. Osteoporos. Rep.* 16 (2018) 423–433. <https://doi.org/10.1007/s11914-018-0454-8>.
- [7] S.R. Goodyear, R.M. Aspden, Mechanical Properties of Bone Ex Vivo, in: R.S. Helfrich M. (Ed.), *Bone Res. Protoc. Methods Mol. Biol. (Methods Protoc. Vol 816., Humana Press, Totowa, NJ, 2012: pp. 555–571*. https://doi.org/10.1007/978-1-61779-415-5_35.
- [8] C. Jelen, G. Mattei, F. Montemurro, C. De Maria, M. Mattioli-Belmonte, G. Vozzi, Bone scaffolds with homogeneous and discrete gradient mechanical properties, *Mater. Sci. Eng. C.* 33 (2013) 28–36. <https://doi.org/10.1016/j.msec.2012.07.046>.

- 1
2
3
4
5 740
6
7
8
9
10
11
12
13
14
15 745
16
17
18
19
20
21
22
23
24 750
25
26
27
28
29
30
31
32
33 755
34
35
36
37
38
39
40
41
42
43 760
44
45
46
47
48
49
50
51
52 765
53
54
55
56
57
58
59
60
61
62
63
64
65
- [9] A. Herrera, J. Hellwig, H. Leemhuis, R. von Klitzing, I. Heschel, G.N. Duda, A. Petersen, From macroscopic mechanics to cell-effective stiffness within highly aligned macroporous collagen scaffolds, *Mater. Sci. Eng. C*. 103 (2019) 109760. <https://doi.org/10.1016/j.msec.2019.109760>.
- [10] H. Jin, W.Y. Lu, S. Scheffel, T.D. Hinnerichs, M.K. Neilsen, Full-field characterization of mechanical behavior of polyurethane foams, *Int. J. Solids Struct.* 44 (2007) 6930–6944. <https://doi.org/10.1016/j.ijsolstr.2007.03.018>.
- [11] P.S.D. Patel, D.E.T. Shepherd, D.W.L. Hukins, Compressive properties of commercially available polyurethane foams as mechanical models for osteoporotic human cancellous bone, *BMC Musculoskelet. Disord.* 9 (2008) 5–11. <https://doi.org/10.1186/1471-2474-9-137>.
- [12] R. Belda, R. Megías, N. Feito, A. Vercher-Martínez, E. Giner, Some practical considerations for compression failure characterization of open-cell polyurethane foams using digital image correlation, *Sensors (Switzerland)*. 20 (2020) 1–21. <https://doi.org/10.3390/s20154141>.
- [13] M.L. Bouxsein, Bone quality: where do we go from here?, *Osteoporos. Int.* 14 (2003) 118–127. <https://doi.org/10.1007/s00198-003-1489-x>.
- [14] T.M. Keaveny, E.F. Morgan, G.L. Niebur, O.C. Yeh, Biomechanics of trabecular bone, *Annu. Rev. Biomed. Eng.* 3 (2001) 307–333. <https://doi.org/10.1146/annurev.bioeng.3.1.307>.
- [15] L. Cristofolini, In vitro evidence of the structural optimization of the human skeletal bones, *J. Biomech.* 48 (2015) 787–796. <https://doi.org/10.1016/j.jbiomech.2014.12.010>.
- [16] S.D. Badilatti, P. Christen, I. Parkinson, R. Müller, Load-adaptive bone remodeling simulations reveal osteoporotic microstructural and mechanical changes in whole human vertebrae, *J. Biomech.* 49 (2016) 3770–3779. <https://doi.org/10.1016/j.jbiomech.2016.10.002>.
- [17] A. Levchuk, A. Zwahlen, C. Weigt, F.M. Lambers, S.D. Badilatti, F.A. Schulte, G. Kuhn, R. Müller, The Clinical Biomechanics Award 2012 - Presented by the European Society of Biomechanics: Large scale simulations of trabecular bone adaptation to loading and treatment, *Clin. Biomech.* 29 (2014) 355–362. <https://doi.org/10.1016/j.clinbiomech.2013.12.019>.
- [18] C.M.J. de Bakker, W.-J. Tseng, Y. Li, H. Zhao, X.S. Liu, Clinical Evaluation of Bone

- 770 Strength and Fracture Risk, *Curr. Osteoporos. Rep.* 15 (2017) 32–42.
1 <https://doi.org/10.1007/s11914-017-0346-3>.
2
3
- [19] G. Graziani, M. Berni, A. Gambardella, M. De Carolis, M.C. Maltarello, M. Boi, G.
4 Carnevale, M. Bianchi, Fabrication and characterization of biomimetic hydroxyapatite
5 thin films for bone implants by direct ablation of a biogenic source, *Mater. Sci. Eng. C.*
6 99 (2019) 853–862. <https://doi.org/10.1016/j.msec.2019.02.033>.
7
8 775
- [20] T.L. Mueller, S.E. Basler, R. Müller, G.H. Van Lenthe, Time-lapsed imaging of implant
9 fixation failure in human femoral heads, *Med. Eng. Phys.* 35 (2013) 636–643.
10 <https://doi.org/10.1016/j.medengphy.2012.07.009>.
11
12
- [21] M. Peña Fernández, F. Witte, G. Tozzi, Applications of X-ray computed tomography
13 for the evaluation of biomaterial-mediated bone regeneration in critical-sized defects,
14 *J. Microsc.* 00 (2019) jmi.12844. <https://doi.org/10.1111/jmi.12844>.
15
16 780
- [22] C.M. Disney, P.D. Lee, J.A. Hoyland, M.J. Sherratt, B.K. Bay, A review of techniques
17 for visualising soft tissue microstructure deformation and quantifying strain Ex Vivo, *J.*
18 *Microsc.* 00 (2018) 1–15. <https://doi.org/10.1111/jmi.12701>.
19
20
- [23] M. Peña Fernández, A.H. Barber, G.W. Blunn, G. Tozzi, A.A. Fern, Optimization of
21 digital volume correlation computation in SR-microCT images of trabecular bone and
22 bone-biomaterial systems, *J. Microsc.* 272 (2018) 213–228.
23 <https://doi.org/10.1111/jmi.12745>.
24
25 785
- [24] E. Dall’Ara, M. Peña-Fernández, M. Palanca, M. Giorgi, L. Cristofolini, G. Tozzi,
26 Precision of DVC approaches for strain analysis in bone imaged with μ CT at different
27 dimensional levels, *Front. Mater.* 4:31 (2017).
28 <https://doi.org/10.3389/fmats.2017.00031>.
29
30 790
- [25] M. Peña Fernández, C. Black, J. Dawson, D. Gibbs, J. Kanczler, R.O.C. Oreffo, G.
31 Tozzi, Exploratory Full-Field Strain Analysis of Regenerated Bone Tissue from
32 Osteoinductive Biomaterials, *Materials (Basel)*. 13 (2020) 168.
33 <https://doi.org/10.3390/ma13010168>.
34
35 795
- [26] C.M. Disney, A. Eckersley, J.C. McConnell, H. Geng, A.J. Bodey, J.A. Hoyland, P.D.
36 Lee, M.J. Sherratt, B.K. Bay, Synchrotron tomography of intervertebral disc
37 deformation quantified by digital volume correlation reveals microstructural influence
38 on strain patterns, *Acta Biomater.* 92 (2019) 290–304.
39 <https://doi.org/https://doi.org/10.1016/j.actbio.2019.05.021>.
40
41 800
- [27] H. Arora, A. Nila, K. Vitharana, J.M. Sherwood, T.T.N. Nguyen, A. Karunaratne, I.K.

- 1
2
3 805 Mohammed, A.J. Bodey, P.J. Hellyer, D.R. Overby, R.C. Schroter, D. Hollis,
4 Microstructural consequences of blast lung injury characterized with digital volume
5 correlation, *Front. Mater.* 4 (2017). <https://doi.org/10.3389/fmats.2017.00041>.
- 6 [28] G. Tozzi, M.P. Fernández, S. Davis, A. Karali, A.P. Kao, G. Blunn, Full-field strain
7 uncertainties and residuals at the cartilage-bone interface in unstained tissues using
8 propagation-based phase-contrast XCT and digital volume correlation, *Materials*
9 (Basel). 13 (2020) 1–15. <https://doi.org/10.3390/ma13112579>.
- 10
11
12
13 810 [29] G. Tozzi, E. Dall, M. Palanca, M. Curto, F. Innocente, L. Cristofolini, Strain
14 uncertainties from two digital volume correlation approaches in prophylactically
15 augmented vertebrae : Local analysis on bone and cement- bone microstructures, *J.*
16 *Mech. Behav. Biomed. Mater.* 67 (2017) 117–126.
17 <https://doi.org/10.1016/j.jmbbm.2016.12.006>.
- 18
19
20
21
22 815 [30] M. Peña Fernández, E. Dall’Ara, A.J. Bodey, R. Parwani, A.H. Barber, G.W. Blunn, G.
23 Tozzi, Full-Field Strain Analysis of Bone–Biomaterial Systems Produced by the
24 Implantation of Osteoregenerative Biomaterials in an Ovine Model, *ACS Biomater.*
25 *Sci. Eng.* 5 (2019) 2543–2554. <https://doi.org/10.1021/acsbiomaterials.8b01044>.
- 26
27
28
29
30
31 820 [31] V. Danesi, G. Tozzi, L. Cristofolini, Application of digital volume correlation to study
32 the efficacy of prophylactic vertebral augmentation, *Clin. Biomech.* 39 (2016) 14–24.
33 <https://doi.org/10.1016/j.clinbiomech.2016.07.010>.
- 34
35
36
37
38
39
40
41 825 [32] A. Nazarian, R. Müller, Time-lapsed microstructural imaging of bone failure behavior,
42 *J. Biomech.* 37 (2004) 55–65. [https://doi.org/10.1016/S0021-9290\(03\)00254-9](https://doi.org/10.1016/S0021-9290(03)00254-9).
- 43
44
45
46
47
48
49
50 830 [33] P.J. Thurner, P. Wyss, R. Voide, M. Stauber, M. Stampanoni, U. Sennhauser, R.
51 Müller, Time-lapsed investigation of three-dimensional failure and damage
52 accumulation in trabecular bone using synchrotron light, *Bone.* 39 (2006) 289–299.
53 <https://doi.org/10.1016/j.bone.2006.01.147>.
- 54
55
56
57
58
59
60 835 [34] D. Huang, Y. Huang, Y. Xiao, X. Yang, H. Lin, G. Feng, X. Zhu, X. Zhang,
61 Viscoelasticity in natural tissues and engineered scaffolds for tissue reconstruction,
62 *Acta Biomater.* 97 (2019) 74–92. <https://doi.org/10.1016/j.actbio.2019.08.013>.
- 63
64
65 [35] D.G. Kim, S.S. Huja, H.R. Lee, B.C. Tee, S. Hueni, Relationships of viscosity with
66 contact hardness and modulus of bone matrix measured by nanoindentation, *J.*
67 *Biomech. Eng.* 132 (2010) 1–5. <https://doi.org/10.1115/1.4000936>.
- [36] M. Unal, A. Creecy, J.S. Nyman, The Role of Matrix Composition in the Mechanical
Behavior of Bone, *Curr. Osteoporos. Rep.* 16 (2018) 205–215.

<https://doi.org/10.1007/s11914-018-0433-0>.

- 1
2 [37] S. Xie, K. Manda, R.J. Wallace, F. Levrero-Florencio, A.H.R.W. Simpson, P. Pankaj,
3 Time Dependent Behaviour of Trabecular Bone at Multiple Load Levels, *Ann. Biomed.*
4 *Eng.* 45 (2017) 1219–1226. <https://doi.org/10.1007/s10439-017-1800-1>.
5
6
7
8 840 [38] K. Manda, R.J. Wallace, S. Xie, F. Levrero-Florencio, P. Pankaj, Nonlinear
9 viscoelastic characterization of bovine trabecular bone, *Environ. Econ. Policy Stud.* 16
10 (2017) 173–189. <https://doi.org/10.1007/s10237-016-0809-y>.
11
12
13 [39] J.Y. Buffiere, E. Maire, J. Adrien, J.P. Masse, E. Boller, In situ experiments with X ray
14 tomography: An attractive tool for experimental mechanics, *Proc. Soc. Exp. Mech.*
15 *Inc.* 67 (2010) 289–305. <https://doi.org/10.1007/s11340-010-9333-7>.
16 845
17
18 [40] E. Maire, P.J. Withers, Quantitative X-ray tomography, *Int. Mater. Rev.* 59 (2014) 1–
19 43. <https://doi.org/10.1179/1743280413Y.0000000023>.
20
21
22 [41] T. De Schryver, M. Dierick, M. Heyndrickx, J. Van Stappen, M.A. Boone, L. Van
23 Hoorebeke, M.N. Boone, Motion compensated micro-CT reconstruction for in-situ
24 analysis of dynamic processes, *Sci. Rep.* 8 (2018) 1–10.
25 850
26 <https://doi.org/10.1038/s41598-018-25916-5>.
27
28 [42] D. Kytýř, P. Zlámal, P. Koudelka, T. Fíla, N. Krčmářová, I. Kumpová, D. Vavřík, A.
29 Gantar, S. Novak, Deformation analysis of gellan-gum based bone scaffold using on-
30 the-fly tomography, *Mater. Des.* 134 (2017) 400–417.
31 855
32 <https://doi.org/10.1016/j.matdes.2017.08.036>.
33
34 [43] T. Bultreys, M.A. Boone, M.N. Boone, T. De Schryver, B. Masschaele, L. Van
35 Hoorebeke, V. Cnudde, Fast laboratory-based micro-computed tomography for pore-
36 scale research: Illustrative experiments and perspectives on the future, *Adv. Water*
37 *Resour.* 95 (2016) 341–351. <https://doi.org/10.1016/j.advwatres.2015.05.012>.
38
39 860 [44] C. Jailin, S. Roux, Dynamic tomographic reconstruction of deforming volumes,
40 *Materials (Basel)*. 11 (2018). <https://doi.org/10.3390/ma11081395>.
41
42 [45] M. Di Michiel, J.M. Merino, D. Fernandez-Carreiras, T. Buslaps, V. Honkimäki, P.
43 Falus, T. Martins, O. Svensson, Fast microtomography using high energy synchrotron
44 radiation, *Rev. Sci. Instrum.* 76 (2005). <https://doi.org/10.1063/1.1884194>.
45
46 865 [46] E. Maire, P.J. Withers, Quantitative X-ray tomography, *Int. Mater. Rev.* 59 (2014) 1–
47 43. <https://doi.org/10.1179/1743280413Y.0000000023>.
48
49 [47] J. Villanova, R. Daudin, P. Lhuissier, D. Jauffrès, S. Lou, C.L. Martin, S. Labouré, R.
50
51
52
53
54
55
56
57
58
59
60
61
62
63
64
65

1 Tucoulou, G. Martínez-Criado, L. Salvo, Fast in situ 3D nanoimaging: a new tool for
2 dynamic characterization in materials science, *Mater. Today*. 20 (2017) 354–359.
3 870 <https://doi.org/10.1016/j.mattod.2017.06.001>.

4
5 [48] A. Nommeots-Nomm, C. Ligorio, A.J. Bodey, B. Cai, J.R. Jones, P.D. Lee, G.
6 Poologasundarampillai, Four-dimensional imaging and quantification of viscous flow
7 sintering within a 3D printed bioactive glass scaffold using synchrotron X-ray
8 tomography, *Mater. Today Adv.* 2 (2019) 100011.
9
10 875 <https://doi.org/10.1016/j.mtadv.2019.100011>.

11
12
13 [49] M. Haug, F. Bouville, J. Adrien, A. Bonnin, E. Maire, A.R. Studart, Multiscale
14 deformation processes during cold sintering of nanovaterite compacts, *Acta Mater.*
15 189 (2020) 266–273. <https://doi.org/10.1016/j.actamat.2020.02.054>.

16
17 [50] Y. Chen, S.J. Clark, C.L.A. Leung, L. Sinclair, S. Marussi, M.P. Olbinado, E. Boller, A.
18 Rack, I. Todd, P.D. Lee, In-situ Synchrotron imaging of keyhole mode multi-layer laser
19 powder bed fusion additive manufacturing, *Appl. Mater. Today*. 20 (2020) 100650.
20 880 <https://doi.org/10.1016/j.apmt.2020.100650>.

21
22 [51] K.M. Kareh, P.D. Lee, R.C. Atwood, T. Connolley, C.M. Gourlay, Revealing the
23 micromechanisms behind semi-solid metal deformation with time-resolved X-ray
24 tomography, *Nat. Commun.* 5 (2014) 1–7. <https://doi.org/10.1038/ncomms5464>.
25 885

26
27 [52] B. Cai, S. Karagadde, L. Yuan, T.J. Marrow, T. Connolley, P.D. Lee, In situ
28 synchrotron tomographic quantification of granular and intragranular deformation
29 during semi-solid compression of an equiaxed dendritic Al-Cu alloy, *Acta Mater.* 76
30 (2014) 371–380. <https://doi.org/10.1016/j.actamat.2014.05.035>.

31
32 [53] W. Wang, E. Guo, A.B. Phillion, D.G. Eskin, T. Wang, P.D. Lee, Semi-solid
33 compression of nano/micro-particle reinforced Al-Cu composites: An in situ
34 synchrotron tomographic study, *Materialia*. 12 (2020).
35 890 <https://doi.org/10.1016/j.mtla.2020.100817>.

36
37 [54] B. Cai, P.D. Lee, S. Karagadde, T.J. Marrow, T. Connolley, Time-resolved
38 synchrotron tomographic quantification of deformation during indentation of an
39 equiaxed semi-solid granular alloy, *Acta Mater.* 105 (2016) 338–346.
40 895 <https://doi.org/10.1016/j.actamat.2015.11.028>.

41
42 [55] M. Peña Fernández, A.P. Kao, F. Witte, H. Arora, G. Tozzi, Low-cycle full-field
43 residual strains in cortical bone and their influence on tissue fracture evaluated via in
44 situ stepwise and continuous X-ray computed tomography, *J. Biomech.* 113 (2020)
45 900

110105. <https://doi.org/10.1016/j.jbiomech.2020.110105>.

- 1
2
3
4
5
6
7
8 905
9
10
11
12
13
14
15
16
17 910
18
19
20
21
22
23
24
25
26 915
27
28
29
30
31
32
33
34
35
36 920
37
38
39
40
41
42
43
44
45 925
46
47
48
49
50
51
52
53
54
55 930
56
57
58
59
60
61
62
63
64
65
- [56] T.M. Keaveny, R.E. Borchers, L.J. Gibson, W.C. Hayes, Trabecular bone modulus and strength can depend on specimen geometry, *J. Biomech.* 26 (1993) 991–1000.
- [57] M. Peña Fernández, E. Dall’Ara, A. Kao, A. Bodey, A. Karali, G. Blunn, A. Barber, G. Tozzi, Preservation of Bone Tissue Integrity with Temperature Control for In Situ SR-MicroCT Experiments, *Materials (Basel)*. 11 (2018) 2155. <https://doi.org/10.3390/ma11112155>.
- [58] M. Peña Fernández, S. Cipiccia, E. Dall’Ara, A.J. Bodey, R. Parwani, M. Pani, G.W. Blunn, A.H. Barber, G. Tozzi, Effect of SR-microCT radiation on the mechanical integrity of trabecular bone using in situ mechanical testing and digital volume correlation, *J. Mech. Behav. Biomed. Mater.* 88 (2018) 109–119. <https://doi.org/10.1016/j.jmbbm.2018.08.012>.
- [59] C. Rau, U. Wagner, Z. Pešić, A. De Fanis, Coherent imaging at the Diamond beamline I13, *Phys. Status Solidi Appl. Mater. Sci.* 208 (2011) 2522–2525. <https://doi.org/10.1002/pssa.201184272>.
- [60] R.C. Atwood, A.J. Bodey, S.W.T. Price, M. Basham, M. Drakopoulos, A high-throughput system for high-quality tomographic reconstruction of large datasets at Diamond Light Source, *Philos. Trans. R. Soc. A Math. Phys. Eng. Sci.* 373 (2015). <https://doi.org/10.1098/rsta.2014.0398>.
- [61] N. Wadeson, M. Basham, Savu: A Python-based, MPI Framework for Simultaneous Processing of Multiple, N-dimensional, Large Tomography Datasets, (2016). <http://arxiv.org/abs/1610.08015>.
- [62] N.T. Vo, R.C. Atwood, M. Drakopoulos, Superior techniques for eliminating ring artifacts in X-ray micro-tomography, *Opt. Express*. 26 (2018) 28396. <https://doi.org/10.1364/oe.26.028396>.
- [63] T. Tanaka, H. Kitamura, SPECTRA: A synchrotron radiation calculation code, *J. Synchrotron Radiat.* 8 (2001) 1221–1228. <https://doi.org/10.1107/S090904950101425X>.
- [64] W.C.W. Chang, T.M. Christensen, T.P. Pinilla, T.M. Keaveny, Uniaxial yield strains for bovine trabecular bone are isotropic and asymmetric, *J. Orthop. Res.* 17 (1999) 582–585. <https://doi.org/10.1002/jor.1100170418>.
- [65] T.M. Wright, W.C. Hayes, Fracture mechanics parameters for compact bone-Effects

of density and specimen thickness, *J. Biomech.* 10 (1977).

[https://doi.org/10.1016/0021-9290\(77\)90019-7](https://doi.org/10.1016/0021-9290(77)90019-7).

- 1
2
3
4 935 [66] J.H. Hubbell, S.. Seltzer, Tables of X-Ray Mass Attenuation Coefficients and Mass
5 Energy-Absorption Coefficients (version 1.4), Natl. Inst. Stand. Technol. Gaithersburg,
6 MD. (2004).
7
8
9
10 [67] D. Mattes, D.R. Haynor, H. Vesselle, T.K. Lewellyn, W. Eubank, Nonrigid
11 multimodality image registration, *Med. Imaging 2001 Image Process.* 4322 (2001)
12 1609–1620. <https://doi.org/10.1117/12.431046>.
13 940
14
15 [68] M. Styner, Parametric estimate of intensity inhomogeneities applied to MRI, *IEEE*
16 *Trans. Med. Imaging.* 19 (2000) 153–165. <https://doi.org/10.1109/42.845174>.
17
18
19 [69] P. Perona, J. Malik, Scale-space and edge detection using anisotropic diffusion, *IEEE*
20 *Trans. Pattern Anal. Mach. Intell.* 12 (1990) 629–639.
21
22 945 <https://doi.org/10.1109/34.56205>.
23
24
25 [70] G. Gerig, O. Kbler, R. Kikinis, F.A. Jolesz, Nonlinear Anisotropic Filtering of MRI Data,
26 *IEEE Trans. Med. Imaging.* 11 (1992) 221–232. <https://doi.org/10.1109/42.141646>.
27
28
29 [71] S. Berg, D. Kutra, T. Kroeger, C.N. Straehle, B.X. Kausler, C. Haubold, M. Schiegg, J.
30 Ales, T. Beier, M. Rudy, K. Eren, J.I. Cervantes, B. Xu, F. Beuttenmueller, A. Wolny,
31 950 C. Zhang, U. Koethe, F.A. Hamprecht, A. Kreshuk, *Ilstik: Interactive Machine*
32 *Learning for (Bio)Image Analysis*, *Nat. Methods.* 16 (2019) 1226–1232.
33 <https://doi.org/10.1038/s41592-019-0582-9>.
34
35
36
37
38 [72] M. Doube, M.M. Klosowski, I. Arganda-Carreras, F.P. Cordelières, R.P. Dougherty,
39 J.S. Jackson, B. Schmid, J.R. Hutchinson, S.J. Shefelbine, *BoneJ: Free and*
40 955 *extensible bone image analysis in ImageJ*, *Bone.* 47 (2010) 1076–1079.
41 <https://doi.org/10.1016/j.bone.2010.08.023>.
42
43
44
45 [73] J. Schindelin, I. Arganda-Carreras, E. Frise, V. Kaynig, M. Longair, T. Pietzsch, S.
46 Preibisch, C. Rueden, S. Saalfeld, B. Schmid, J.-Y. Tinevez, D.J. White, V.
47 Hartenstein, K. Eliceiri, P. Tomancak, A. Cardona, *Fiji: an open-source platform for*
48 *biological-image analysis*, *Nat Meth.* 9 (2012) 676–682.
49 960 <https://doi.org/10.1038/nmeth.2019>.
50
51
52
53
54 [74] M. Peña Fernández, A.H. Barber, G.W. Blunn, G. Tozzi, Optimization of digital
55 volume correlation computation in SR-microCT images of trabecular bone and bone-
56 biomaterial systems, *J. Microsc.* 272 (2018) 213–228.
57 965 <https://doi.org/10.1111/jmi.12745>.
58
59
60
61
62
63
64
65

- 1
2
3
4
5
6
7 970 [75] M. Palanca, G. Tozzi, L. Cristofolini, M. Viceconti, E. Dall'Ara, Three-Dimensional
8 Local Measurements of Bone Strain and Displacement: Comparison of Three Digital
9 Volume Correlation Approaches, *J. Biomech. Eng.* 137 (2015) 1–14.
10 <https://doi.org/10.1115/1.4030174>.
11
12
13
14
15
16 975 [76] M. Palanca, L. Cristofolini, E. Dall'Ara, M. Curto, F. Innocente, V. Danesi, G. Tozzi,
17 Digital volume correlation can be used to estimate local strains in natural and
18 augmented vertebrae: an organ-level study, *J. Biomech.* 49 (2016) 3882–3890.
19 <https://doi.org/10.1016/j.jbiomech.2016.10.018>.
20
21
22 [77] L. North, D. Labonte, M.L. Oyen, M.P. Coleman, H.B. Caliskan, R.E. Johnston,
23 Interrelated chemical-microstructural-nanomechanical variations in the structural units
24 of the cuttlebone of *Sepia officinalis*, *APL Mater.* 5 (2017) 116103.
25 <https://doi.org/10.1063/1.4993202>.
26
27
28 [78] G. Tozzi, V. Danesi, M. Palanca, L. Cristofolini, Elastic Full-Field Strain Analysis and
29 Microdamage Progression in the Vertebral Body from Digital Volume Correlation,
30 *Strain.* 52 (2016) 446–455. <https://doi.org/10.1111/str.12202>.
31
32
33 980 [79] F. Gillard, R. Boardman, M. Mavrogordato, D. Hollis, I. Sinclair, F. Pierron, M.
34 Browne, The application of digital volume correlation (DVC) to study the
35 microstructural behaviour of trabecular bone during compression, *J. Mech. Behav.*
36 *Biomed. Mater.* 29 (2014) 480–499. <https://doi.org/10.1016/j.jmbbm.2013.09.014>.
37
38
39 985 [80] B.K. Bay, T.S. Smith, D.P. Fyhrie, M. Saad, Digital volume correlation: Three-
40 dimensional strain mapping using X-ray tomography, *Exp. Mech.* 39 (1999) 217–226.
41 <https://doi.org/10.1007/BF02323555>.
42
43
44 990 [81] M. Peña Fernández, E. Dall'Ara, A.J. Bodey, R. Parwani, A.H. Barber, G.W. Blunn, G.
45 Tozzi, Full-Field Strain Analysis of Bone-Biomaterial Systems Produced by the
46 Implantation of Osteoregenerative Biomaterials in an Ovine Model, *ACS Biomater.*
47 *Sci. Eng.* 5 (2019) 2543–2554. <https://doi.org/10.1021/acsbiomaterials.8b01044>.
48
49
50 [82] E. Dall'Ara, D. Barber, M. Viceconti, About the inevitable compromise between spatial
51 resolution and accuracy of strain measurement for bone tissue: A 3D zero-strain
52 study, *J. Biomech.* 47 (2014) 2956–2963.
53 <https://doi.org/10.1016/j.jbiomech.2014.07.019>.
54 995
55
56 [83] H.H. Bayraktar, E.F. Morgan, G.L. Niebur, G.E. Morris, E.K. Wong, T.M. Keaveny,
57 Comparison of the elastic and yield properties of human femoral trabecular and
58 cortical bone tissue, *J. Biomech.* 37 (2004) 27–35. <https://doi.org/10.1016/S0021->
59
60
61
62
63
64
65

9290(03)00257-4.

- 1
2 1000 [84] G.L. Niebur, M.J. Feldstein, J.C. Yuen, T.J. Chen, T.M. Keaveny, High-resolution
3 finite element models with tissue strength asymmetry accurately predict failure of
4 trabecular bone, *J. Biomech.* 33 (2000) 1575–1583. [https://doi.org/10.1016/S0021-](https://doi.org/10.1016/S0021-9290(00)00149-4)
5 [9290\(00\)00149-4](https://doi.org/10.1016/S0021-9290(00)00149-4).
6
7
8
9
10 [85] M.J. Turunen, S. Le Cann, E. Tudisco, G. Lovric, A. Patera, S.A. Hall, H. Isaksson,
11 1005 Sub-trabecular strain evolution in human trabecular bone, *Sci. Rep.* 10 (2020) 1–14.
12 <https://doi.org/10.1038/s41598-020-69850-x>.
13
14
15 [86] E.N. Cresswell, T.M. Nguyen, M.W. Horsfield, A.J. Alepuz, T.A. Metzger, G.L. Niebur,
16 C.J. Hernandez, Mechanically induced bone formation is not sensitive to local
17 osteocyte density in rat vertebral cancellous bone, *J. Orthop. Res.* 36 (2018) 672–
18 681. <https://doi.org/10.1002/jor.23606>.
19
20 1010
21
22 [87] D. Christen, A. Levchuk, S. Schori, P. Schneider, S.K. Boyd, R. Müller, Deformable
23 image registration and 3D strain mapping for the quantitative assessment of cortical
24 bone microdamage, *J. Mech. Behav. Biomed. Mater.* 8 (2012) 184–193.
25 <https://doi.org/10.1016/j.jmbbm.2011.12.009>.
26
27
28
29
30 1015 [88] M. Peña Fernández, E. Dall’Ara, A.P. Kao, A.J. Bodey, A. Karali, G.W. Blunn, A.H.
31 Barber, G. Tozzi, Preservation of bone tissue integrity with temperature control for in
32 situ SR-microCT experiments, *Materials (Basel)*. (2018). <https://doi.org/under review>.
33
34
35 [89] M.J. Mirzaali, J.J. Schwiedrzik, S. Thaiwichai, J.P. Best, J. Michler, P.K. Zysset, U.
36 Wolfram, Mechanical properties of cortical bone and their relationships with age,
37 gender, composition and microindentation properties in the elderly, *Bone*. 93 (2016)
38 196–211. <https://doi.org/10.1016/j.bone.2015.11.018>.
39 1020
40
41
42 [90] G. Benecke, M. Kerschnitzki, P. Fratzl, H.S. Gupta, Digital image correlation shows
43 localized deformation bands in inelastic loading of fibrolamellar bone, *J. Mater. Res.*
44 24 (2009) 421–429. <https://doi.org/10.1557/jmr.2009.0064>.
45
46
47
48
49 1025 [91] X.S. Liu, G. Bevill, T.M. Keaveny, P. Sajda, X.E. Guo, Micromechanical analyses of
50 vertebral trabecular bone based on individual trabeculae segmentation of plates and
51 rods, *J. Biomech.* 42 (2009) 249–256. <https://doi.org/10.1016/j.jbiomech.2008.10.035>.
52
53
54 [92] M. Zedda, R. Babosova, Does the osteon morphology depend on the body mass? A
55 scaling study on macroscopic and histomorphometric differences between cow (*Bos*
56 *taurus*) and sheep (*Ovis aries*), *Zoomorphology*. 140 (2021) 169–181.
57
58 1030
59 <https://doi.org/10.1007/s00435-021-00516-6>.
60
61
62
63
64
65

- 1
2
3
4
5 1035
6
7
8
9
10
11
12
13
14
15 1040
16
17
18
19
20
21
22
23
24 1045
25
26
27
28
29
30
31
32
33
34 1050
35
36
37
38
39
40
41
42
43 1055
44
45
46
47
48
49
50
51
52 1060
53
54
55
56
57
58
59
60
61
62
63
64
65
- [93] H.D. Barth, E.A. Zimmermann, E. Schaible, S.Y. Tang, T. Alliston, R.O. Ritchie, Characterization of the effects of x-ray irradiation on the hierarchical structure and mechanical properties of human cortical bone, *Biomaterials*. 32 (2011) 8892–8904. <https://doi.org/10.1016/j.biomaterials.2011.08.013>.
- [94] H.D. Barth, M.E. Launey, A.A. MacDowell, J.W. Ager, R.O. Ritchie, On the effect of X-ray irradiation on the deformation and fracture behavior of human cortical bone, *Bone*. 46 (2010) 1475–1485. <https://doi.org/10.1016/j.bone.2010.02.025>.
- [95] O. Paris, From diffraction to imaging: New avenues in studying hierarchical biological tissues with x-ray microbeams (Review), *Biointerphases*. 3 (2008) FB16–FB26. <https://doi.org/10.1116/1.2955443>.
- [96] T.L. Norman, E.S. Ackerman, T.S. Smith, T.A. Gruen, A.J. Yates, J.D. Blaha, V.L. Kish, Cortical Bone Viscoelasticity and Fixation Strength of Press-Fit Femoral Stems: An In-Vitro Model, *J. Biomech. Eng.* 128 (2005) 13–17. <https://doi.org/10.1115/1.2133766>.
- [97] M. Taylor, J. Cotton, P. Zioupos, Finite element simulation of the fatigue behaviour of cancellous bone, *Meccanica*. 37 (2002) 419–429. <https://doi.org/10.1023/A:1020848007201>.
- [98] A. Phillips, P. Pankaj, F. May, K. Taylor, C. Howie, A. Usmani, Constitutive models for impacted morsellised cortico-cancellous bone, *Biomaterials*. 27 (2006) 2162–2170. <https://doi.org/10.1016/j.biomaterials.2005.10.034>.
- [99] P. Pollintine, J. Luo, B. Offa-Jones, P. Dolan, M.A. Adams, Bone creep can cause progressive vertebral deformity, *Bone*. 45 (2009) 466–472. <https://doi.org/10.1016/j.bone.2009.05.015>.
- [100] C. Sandino, D.D. McErlain, J. Schipilow, S.K. Boyd, The poro-viscoelastic properties of trabecular bone: A micro computed tomography-based finite element study, *J. Mech. Behav. Biomed. Mater.* 44 (2015) 1–9. <https://doi.org/10.1016/j.jmbbm.2014.12.018>.
- [101] X. Zhai, J. Gao, Y. Nie, Z. Guo, N. Kedir, B. Claus, T. Sun, K. Fezzaa, X. Xiao, W.W. Chen, Real-time visualization of dynamic fractures in porcine bones and the loading-rate effect on their fracture toughness, *J. Mech. Phys. Solids*. 131 (2019) 358–371. <https://doi.org/10.1016/j.jmps.2019.07.010>.

1
2
3
4
5
6
7
8
9
10
11
12
13
14
15
16
17
18
19
20
21
22
23
24
25
26
27
28
29
30
31
32
33
34
35
36
37
38
39
40
41
42
43
44
45
46
47
48
49
50
51
52
53
54
55
56
57
58
59
60
61
62
63
64
65

Table 1. Summary of imaging settings used for the acquisition of SR-microCT images for each material type, including closed-cell (PCF20) and open-cell (PCF15) polyurethane foam, Mg-based open porous scaffold (Mg), trabecular bone (TB), cortical bone (CB) and cuttlebone (CF, cuttlefish bone). n: number of specimens tested per material type.

Table 2. Summary of DVC multipass scheme used for each material and corresponding displacement and strain errors for the n number of specimens analysed for closed-cell (PCF20) and open-cell (PCF15) polyurethane foam, Mg-based open porous scaffold (Mg), trabecular bone (TB), cortical bone (CB) and cuttlebone (CF, cuttlefish bone). Errors are reported as mean (standard deviation) for both MAER and SDER among the n specimens per material.

Table 3. Summary of the morphological parameters of the analysed biostructures including closed-cell (PCF20) and open-cell (PCF15) polyurethane foam, Mg-based open porous scaffold (Mg), trabecular bone (TB), cortical bone (CB) and cuttlebone (CF, cuttlefish bone). For each material, solid volume fraction (SV_f), thickness and spacing are reported as mean (standard deviation) among the n specimens per material.

Video S1. DVC-computed 4D strain distribution in PCF20 closed-cell foams subjected to time-lapsed *in situ* SR-microCT compression (i.e., 1%, 2% and 3% applied compression).

Video S2. DVC-computed 4D strain distribution in PCF20 closed-cell foams subjected to time-resolved continuous *in situ* SR-microCT mechanics up to ~6% apparent compression.

Video S3. DVC-computed 4D strain distribution in PCF15 cellular open foams subjected to time-lapsed *in situ* SR-microCT compression (i.e., 1%, 2% and 3% applied compression).

Video S4. DVC-computed 4D strain distribution in PCF15 cellular open foams subjected to time-resolved continuous *in situ* SR-microCT mechanics up to ~6.5% apparent compression. White ovals in PCF15#4 and PCF15#6 indicate regions where failure occurred, followed by strain redistribution.

Video S5. DVC-computed 4D strain distribution in Mg-based scaffolds subjected to time-resolved continuous *in situ* SR-microCT mechanics up to ~10-14% apparent compression.

Video S6. DVC-computed 4D strain distribution in trabecular bone specimens subjected to time-resolved continuous *in situ* SR-microCT compression up to failure. White ovals indicate failure regions, which occurred first in rod-like structures compared to plate-like structures. Trabecular rods seemed to undertake higher strain levels prior to fracture compare to trabecular plates.

Video S7. DVC-computed 4D strain distribution in cortical bone specimens subjected to time-resolved continuous *in situ* SR-microCT compression up to failure. White arrows indicate location of cracks in correspondence with highly-strained regions.

Video S8. DVC-computed 4D strain distribution in cuttlebone specimen subjected to time-resolved continuous *in situ* SR-microCT mechanics up to ~27% apparent compression.

Figure 1. Reconstructed SR-microCT volumes of the specimens tested. (a) Closed-cell foam (Sawbones PCF20), (b) open-cell foam (Sawbones PCF15), (c) Mg-based open porous scaffold (d) cortical bone, (e) trabecular bone and (f) cuttlebone. SR-microCT images were acquired with a (a, b, d, e) 6.5 μm , (c) 10.4 μm and (e) 5.2 μm isotropic voxel size.

Figure 2. Analysis of SR-microCT images acquired during static and dynamic conditions. A representative SR-microCT cross-section is shown for (a) open-cell foam PCF15, (b) cortical bone and (c) cuttlebone while imaging was performed statically (I), and dynamically during the linear loading regime (II) and mechanical failure (III). (IV) Normalised histograms of the zoomed-in regions in (I-III). Normalisation was performed with respect to the mode (e.g., most frequent) values of each histogram. Scale bars: 500 μm .

Figure 3. *In situ* SR-microCT compression of PCF20 closed-cell foams subjected to time-lapsed (#1-3) or continuous (#4-6) compression. (a) Force-compression curves for the six specimens. For specimens #1 to #3 the force shows a drop at the end of each compression step, corresponding to the time the specimens were allowed to settle prior to SR-microCT imaging; unloading part of the curve after 3% compression is also shown. (b) DVC-computed minimum principal strains (ϵ_{p3}) at each step (i.e., following each acquired tomogram) in relation to the applied deformation. The solid-dashed lines represent the mean ϵ_{p3} values, with the shaded areas and error bars representing the standard deviation over the entire specimen volume. The 3D full-field third principal strain distribution (ϵ_{p3}) at 1%, 2% and 3% applied compression is visualised for (c) PCF20#3 and (d) PCF20#5 specimens, with specimen-dependent colour-coded bounding boxes as in (a) and (b). The 4D strain distribution for all specimens can be found in Videos S1 and S2. *The applied compression for the specimens imaged dynamically was estimated from the actuator speed, imaging time and delay between each pair of consecutive tomograms.

Figure 4. *In situ* SR-microCT compression of PCF15 cellular open foams subjected to time-lapsed (#1-3) or continuous (#4-6) compression. (a) Force-compression curves for the six specimens. For specimens #1 to #3 the force shows a drop at the end of each compression step, corresponding to the time the specimens were allowed to settle prior to SR-microCT imaging; unloading part of the curve after 3% compression is also shown. (b) DVC-computed minimum principal strains (ϵ_{p3}) at each step (i.e., following each acquired tomogram) in relation to the applied deformation. The solid-dashed lines represent the mean ϵ_{p3} values, with the shaded areas and error bars representing the standard deviation over the entire specimen volume. The 3D full-field third principal strain distribution (ϵ_{p3}) at 1%, 2% and 3% applied compression is visualised for (c) PCF15#1 and (d) PCF15#5 specimens, with specimen-dependent colour-coded bounding boxes as in (a) and (b). The 4D strain distribution for all specimens can be found in Videos S3 and S4. *The applied compression for the specimens imaged dynamically was estimated from the actuator speed, imaging time and delay between each pair of consecutive tomograms.

Figure 5. Local failure tracking in a region of interest of PCF15#6. The 3D full-field third principal strain distribution (ϵ_{p3}) at the selected time-points in (a) are represented. Arrows indicate regions of maximum local strains where failure occurred, with blue arrows indicating the first failure event and green arrows the next collapsed regions.

Figure 6. *In situ* SR-microCT compression of Mg-based scaffolds undergoing continuous compression. (a) Force-compression curves for the three specimens. (b) DVC-computed minimum principal strains (ϵ_{p3}) at each step (i.e., following each acquired tomogram) in relation to the applied deformation. The solid lines represent the mean ϵ_{p3} values, with the shaded areas representing the standard deviation over the entire specimen volume. The 3D full-field third principal strain distribution (ϵ_{p3}) at 3%, 7% and 10% compression are visualised for (c) the entire volume of Mg#2 specimen and (d) a magnified region of interest with white area indicating localised impingement of the fibers next to highly strained regions. (e) Colour-coded fibre spacing (i.e., negative space of the fibres) in the same region of interest of (d) with white ovals indicating pores closing. The 4D strain distribution for all specimens can

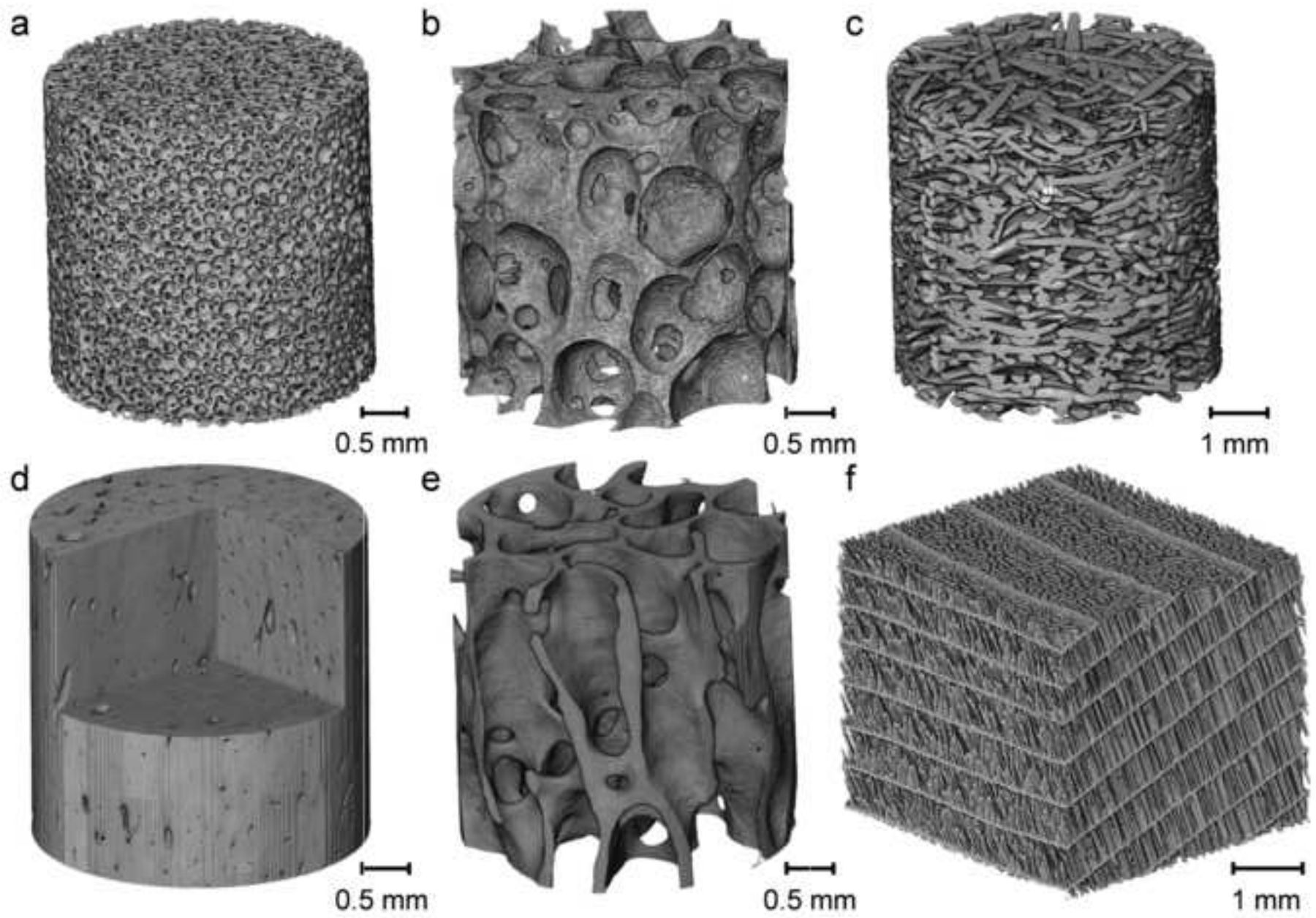
be found in Video S5. *The applied compression was estimated from the actuator speed, imaging time and delay between each pair of consecutive tomograms.

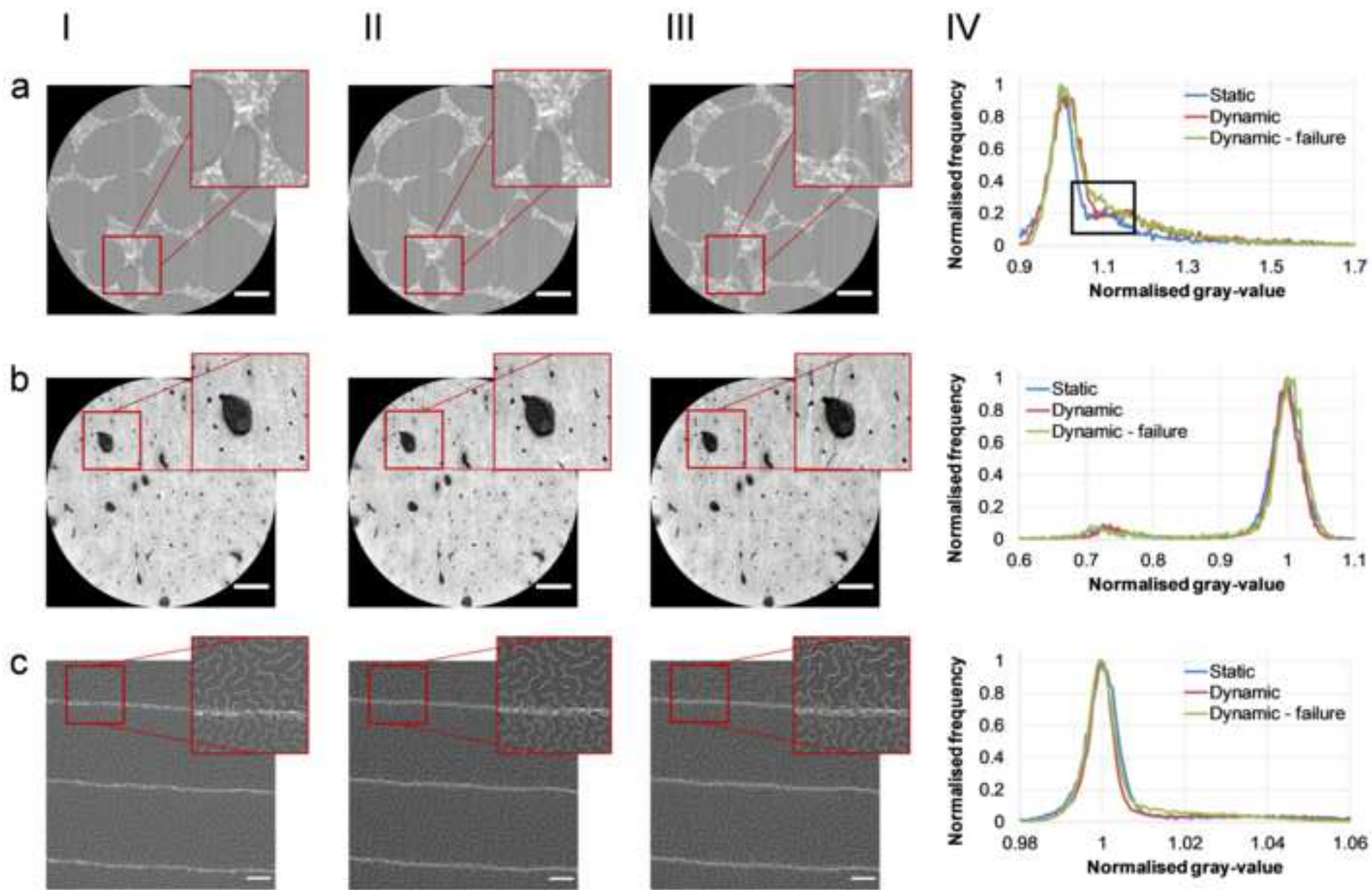
Figure 7. *In situ* SR-microCT compression of trabecular bone (TB) structures undergoing continuous compression. (a) Force-compression curves for the five tested specimens. (b) DVC-computed minimum principal strains (ϵ_{p3}) at each step (i.e., following each acquired tomogram) in relation to the applied deformation. The solid lines represent the mean ϵ_{p3} values, with the shaded areas representing the standard deviation over the entire specimen volume. x symbols in the insert indicate step prior to cracking. The 3D full-field third principal strain distribution (ϵ_{p3}) before, during and after failure is visualised for (c) TB#4 (rod-like structure) and (d) TB#2 (plate-like structure) specimens, with specimen-dependent colour-coded bounding boxes as in (a) and (b). Arrows indicate highly strained regions tracked over time where cracks in the structure appeared. The 4D strain distribution for all specimens can be found in Video S6. *The applied compression was estimated from the actuator speed, imaging time and delay between each pair of consecutive tomograms.

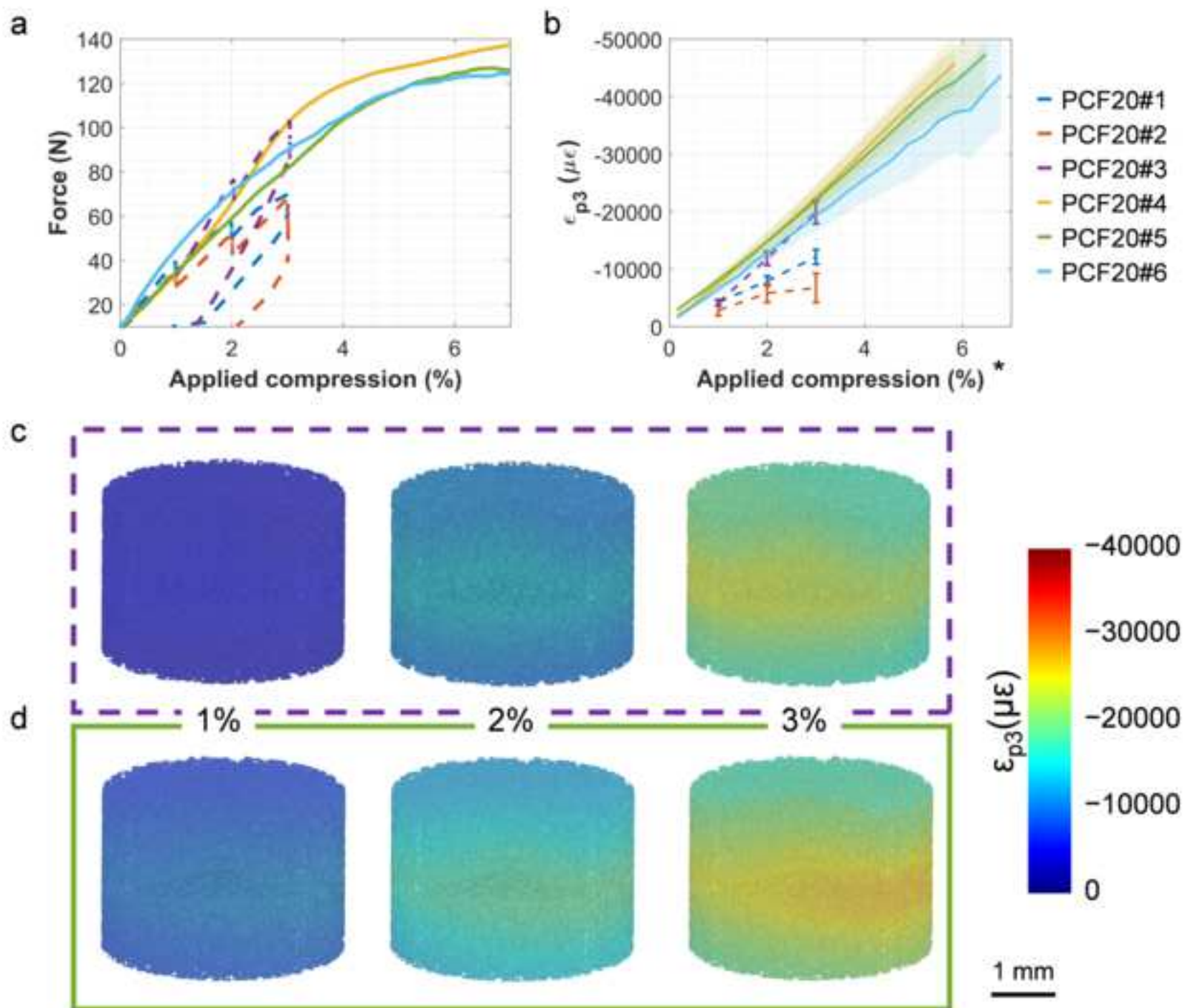
Figure 8. *In situ* SR-microCT compression of cortical bone (CB) structures undergoing continuous compression. (a) Force-compression curves for the four tested specimens. (b) DVC-computed minimum principal strains (ϵ_{p3}) at each step (i.e., following each acquired tomogram) in relation to the applied deformation. The solid lines represent the mean ϵ_{p3} values, with the shaded areas representing the standard deviation over the entire specimen volume. x symbols in the insert indicate step prior to cracking. The 3D full-field third principal strain distribution (ϵ_{p3}) before, during and after failure is visualised for (c) CB#1 and (d) CB#4 specimens, with specimen-dependent colour-coded bounding boxes as in (a) and (b). Arrows indicate highly strained regions tracked over time where cracks in the structure appeared. The 4D strain distribution for all specimens can be found in Video S7. *The applied compression was estimated from the actuator speed, imaging time and delay between each pair of consecutive tomograms.

Figure 9. Crack initiation and propagation in CB#5 cortical bone specimen. (a) Some cracks initiated next to a Haversian canal (green arrow), in the more strained regions (Figure 8c). (b, c) Larger cracks promoting structural failure as a result of strain heterogeneity (Fig. 8d) showed a deviation among the osteons during propagation (orange arrow). Scale bars: 500 μm .

Figure 10. *In situ* SR-microCT compression of cuttlebone (CF) structure undergoing continuous compression. (a) Force-compression curves for the tested specimen. (b) DVC-computed minimum principal strains (ϵ_{p3}) at each step (i.e., following each acquired tomogram) in relation to the applied deformation. The solid lines represent the mean ϵ_{p3} values, with the shaded areas representing the standard deviation over the entire specimen volume. (c) The 3D full-field third principal strain distribution (ϵ_{p3}) at the compression levels denoted by the symbols. Arrows indicate highly strained regions tracked in the pillars over time where collapse was observed. The 4D strain distribution can be found in Video S8. *The applied compression was estimated from the actuator speed, imaging time and delay between each pair of consecutive tomograms.







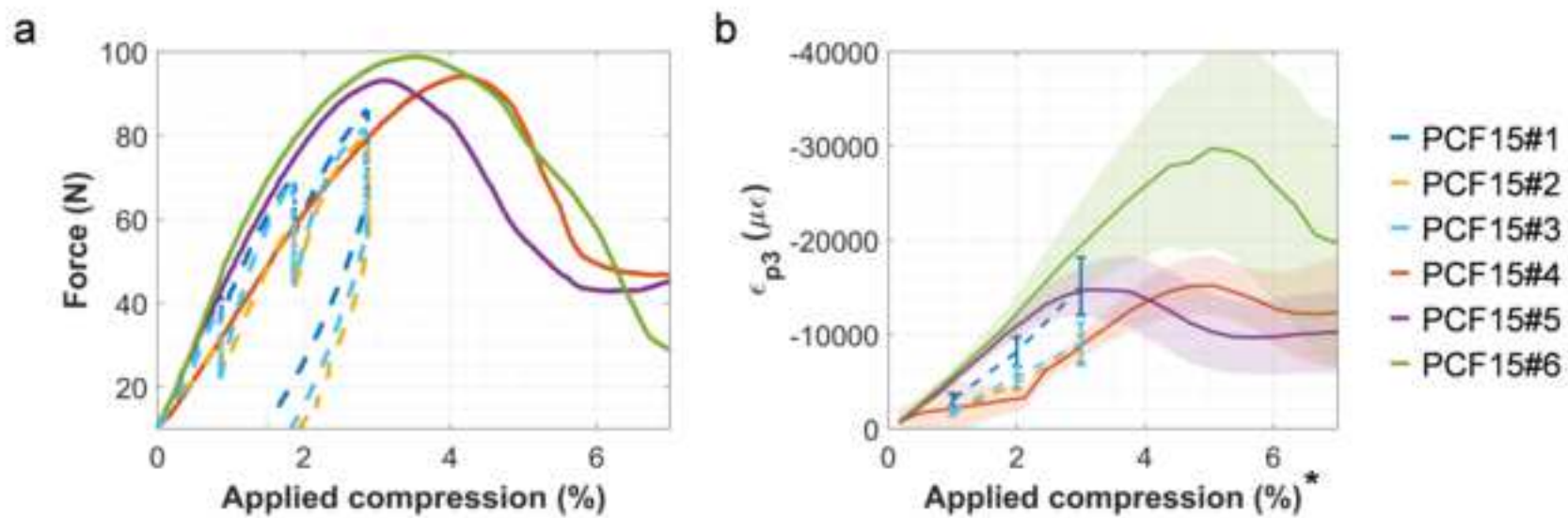
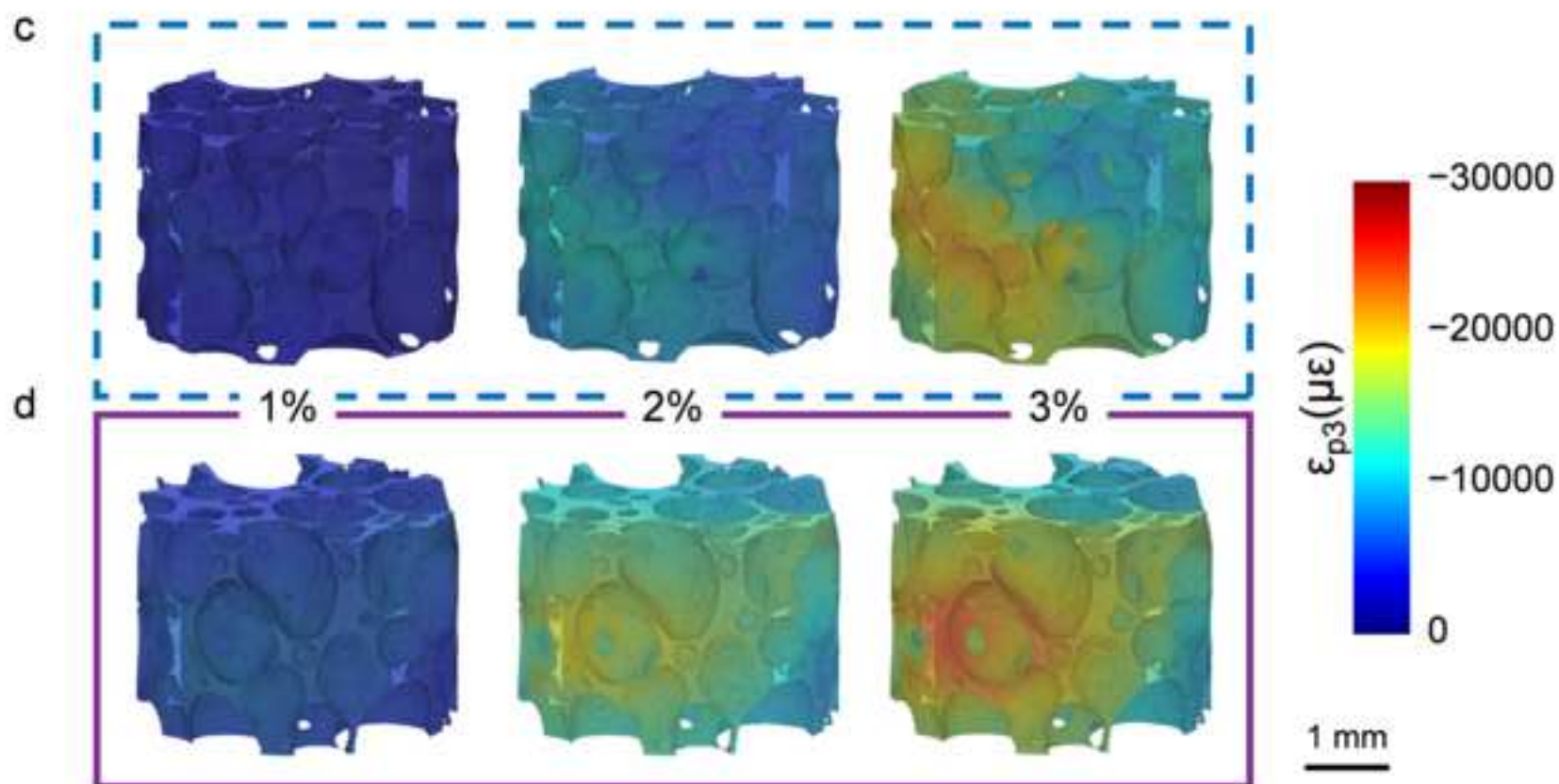
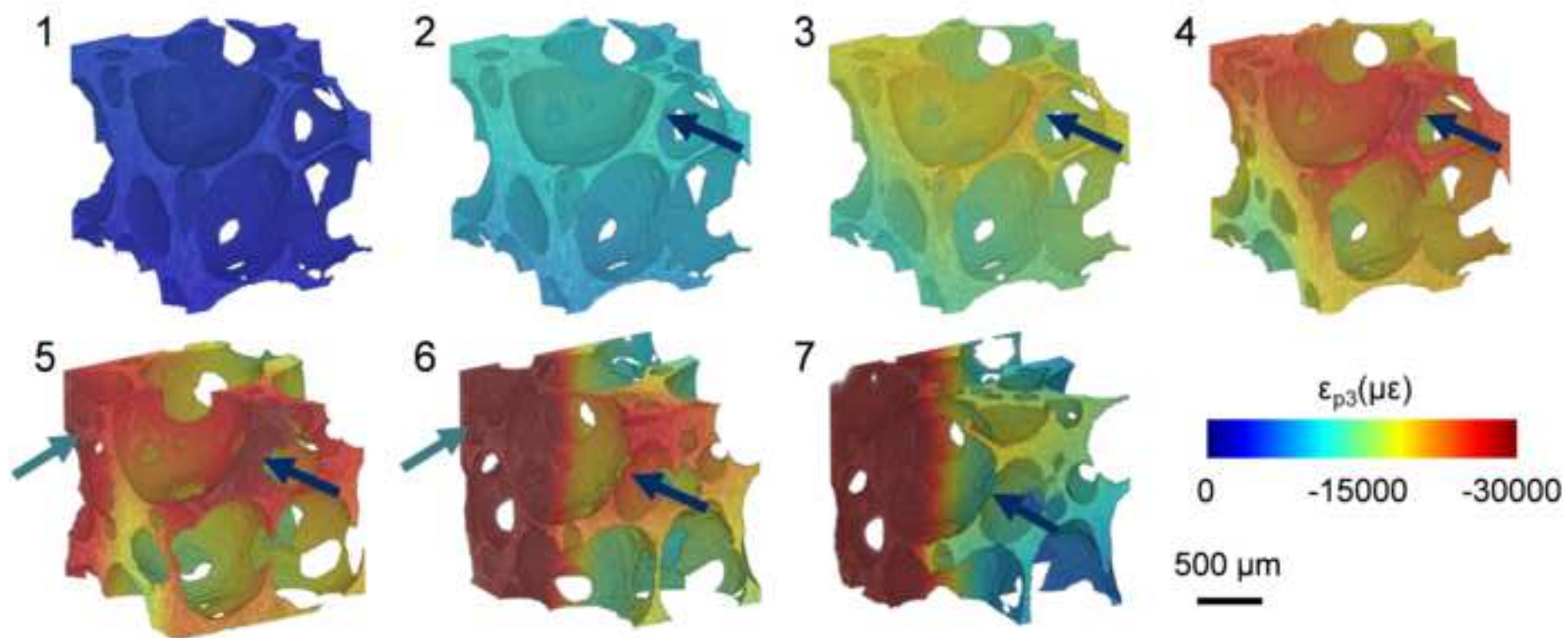
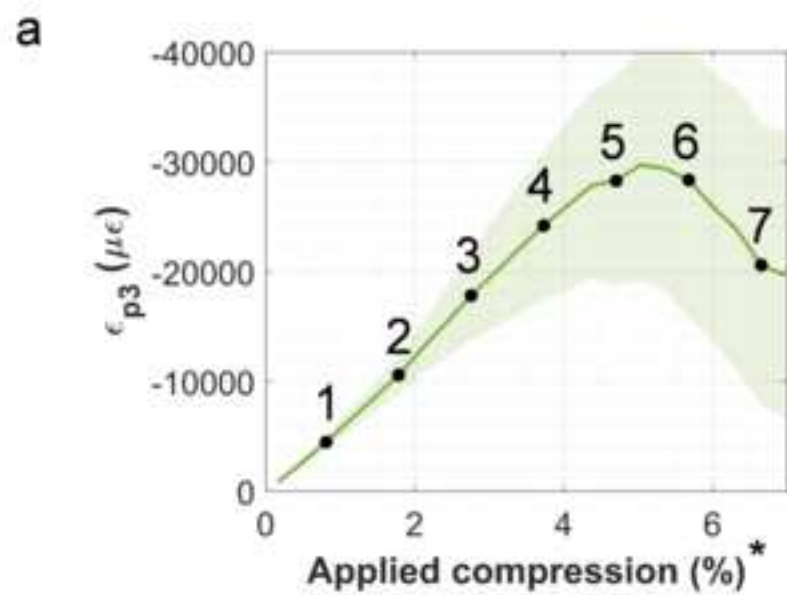


Figure4.png





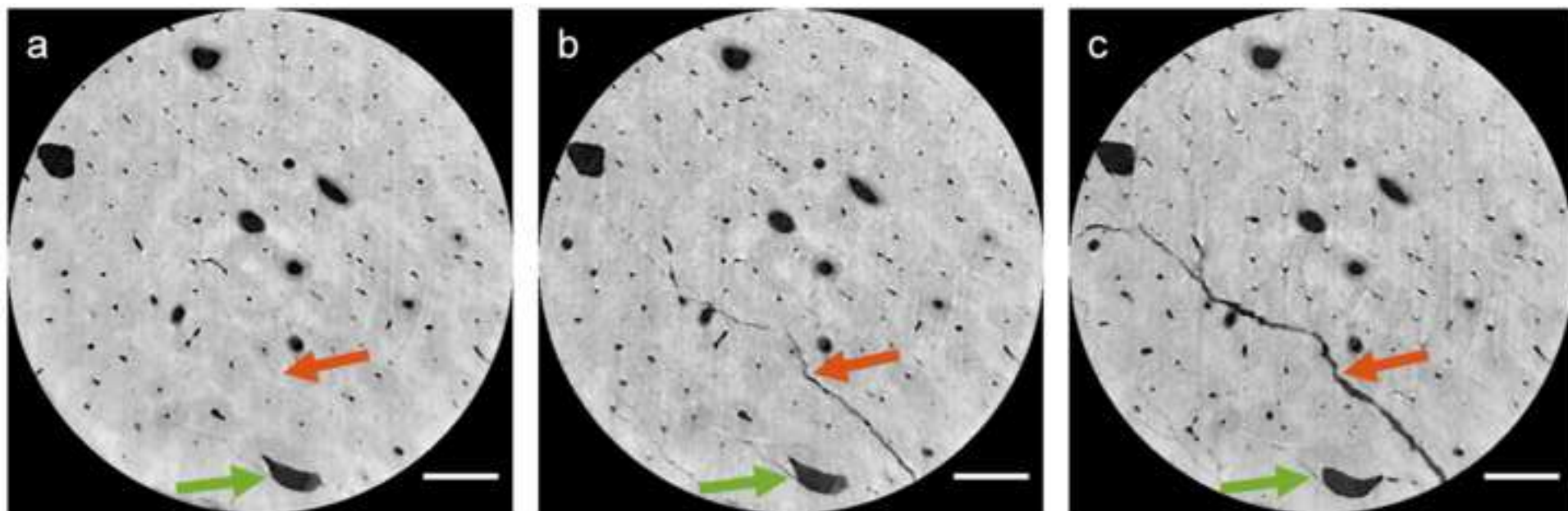
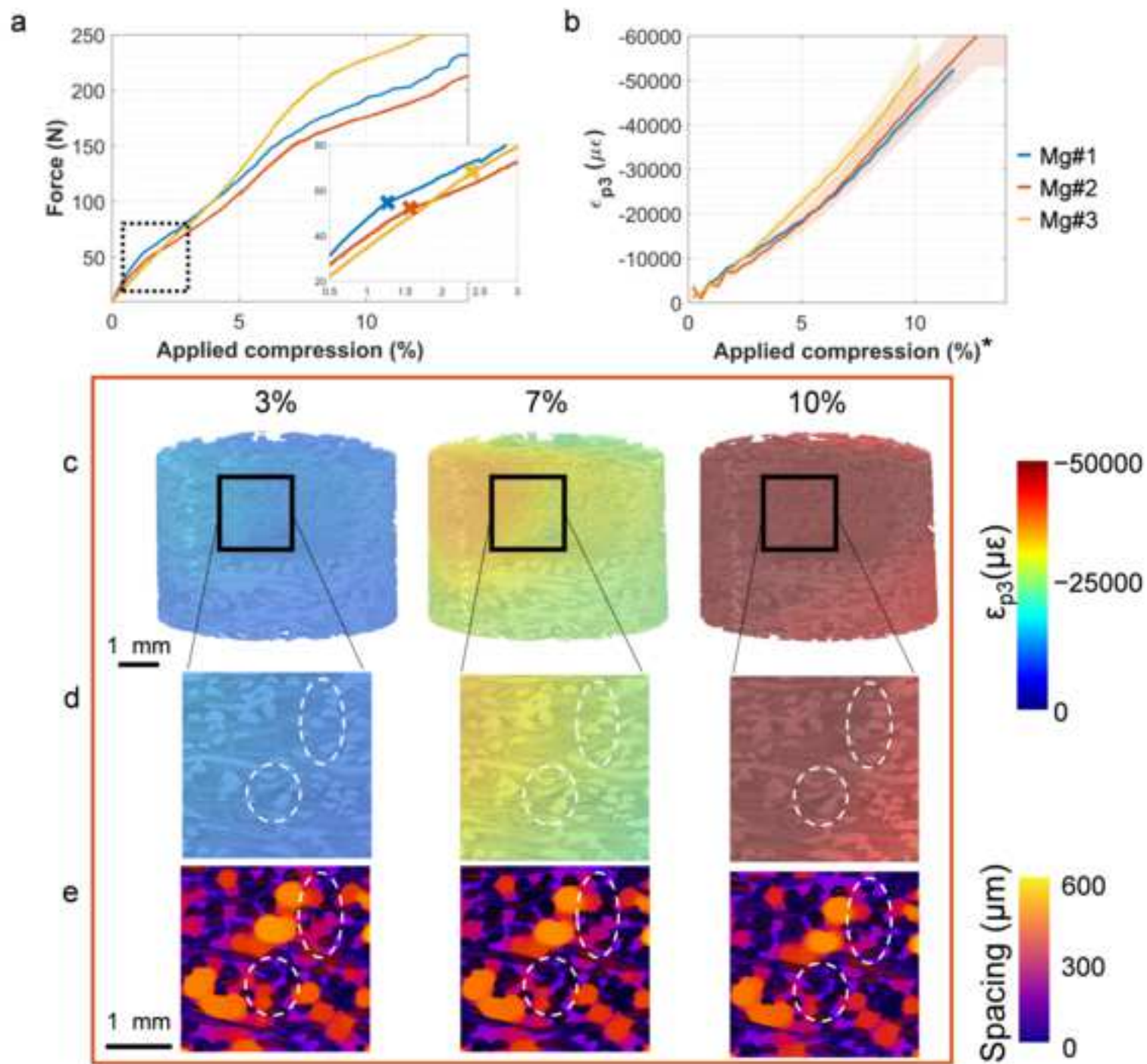
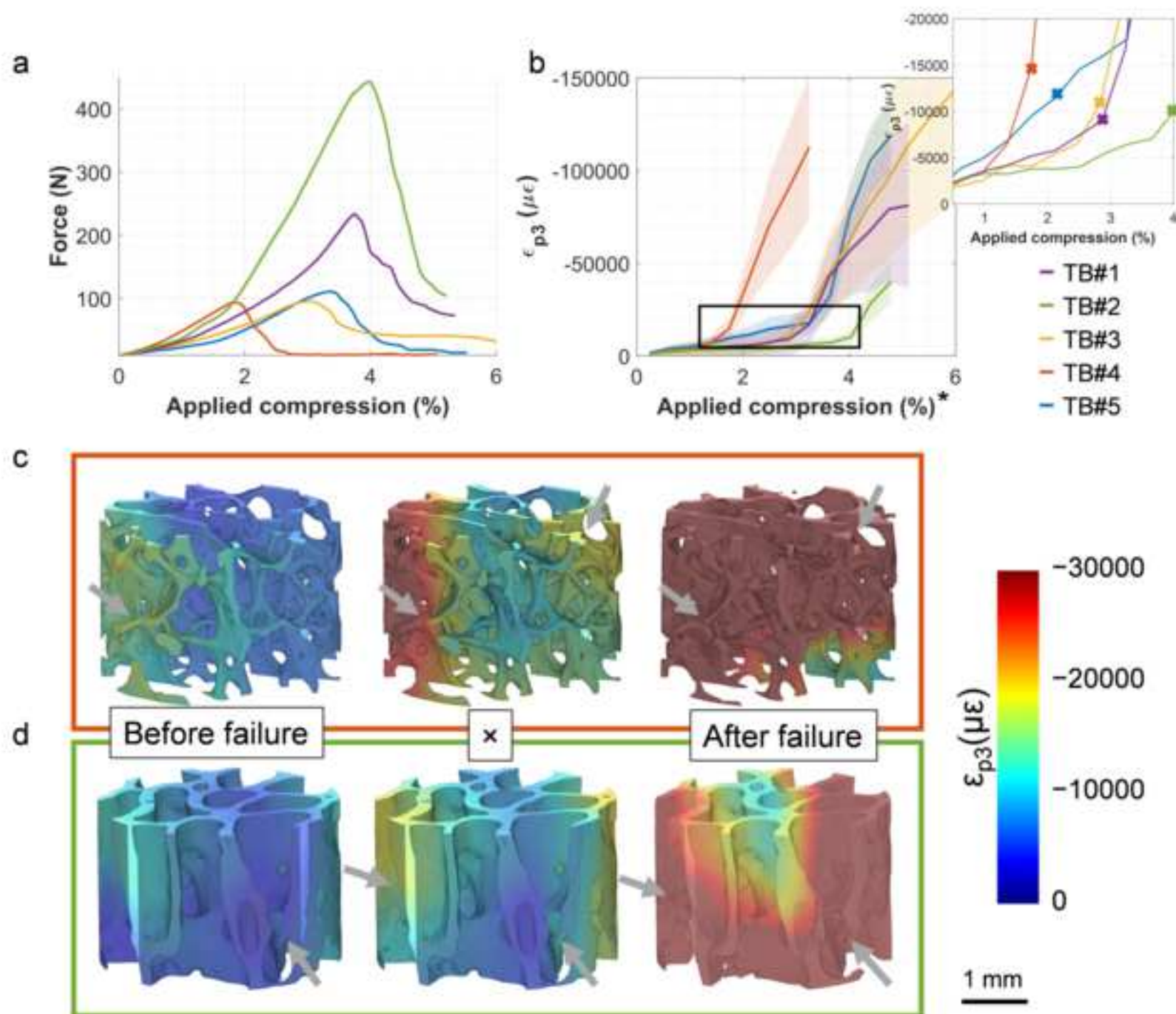
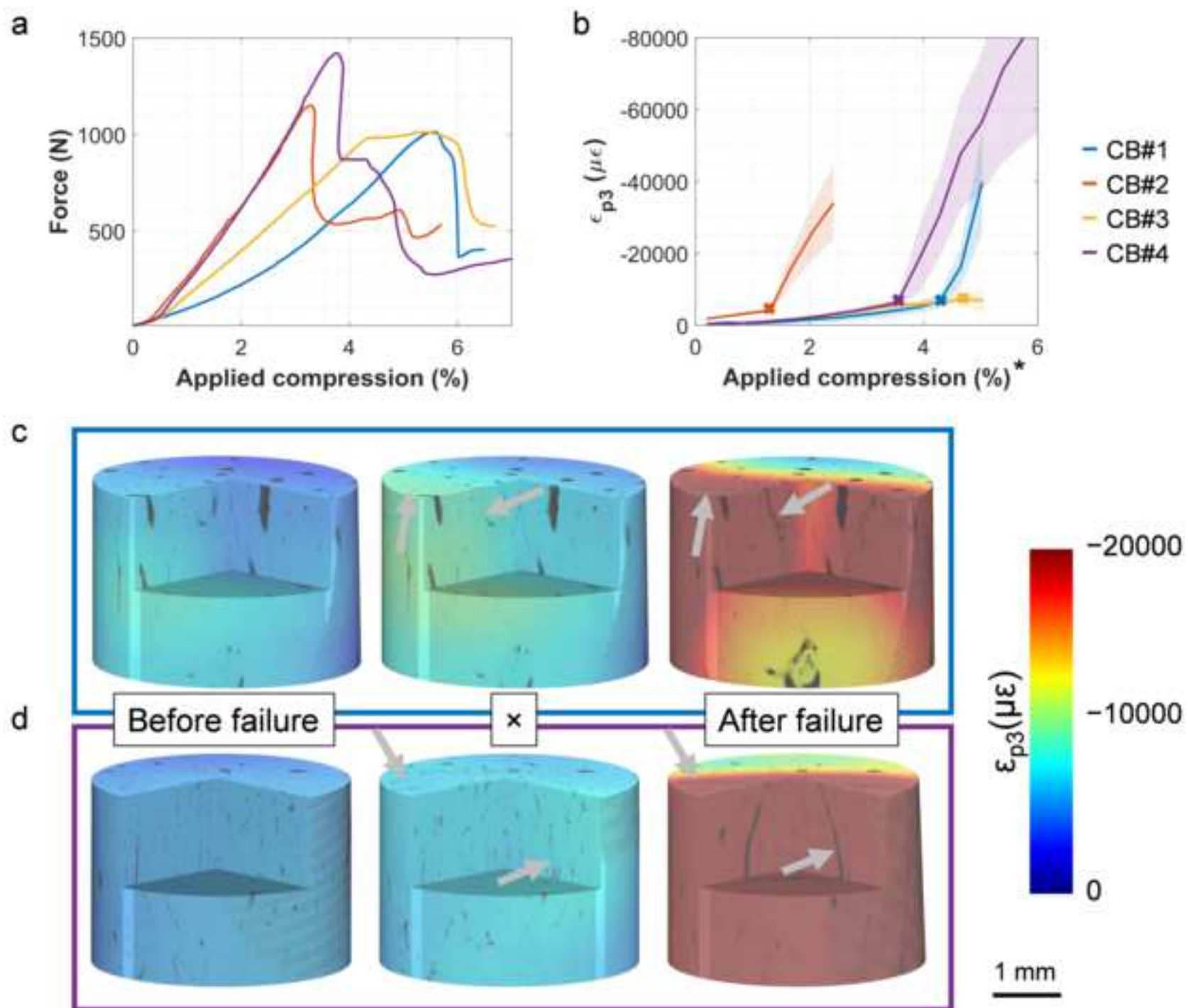
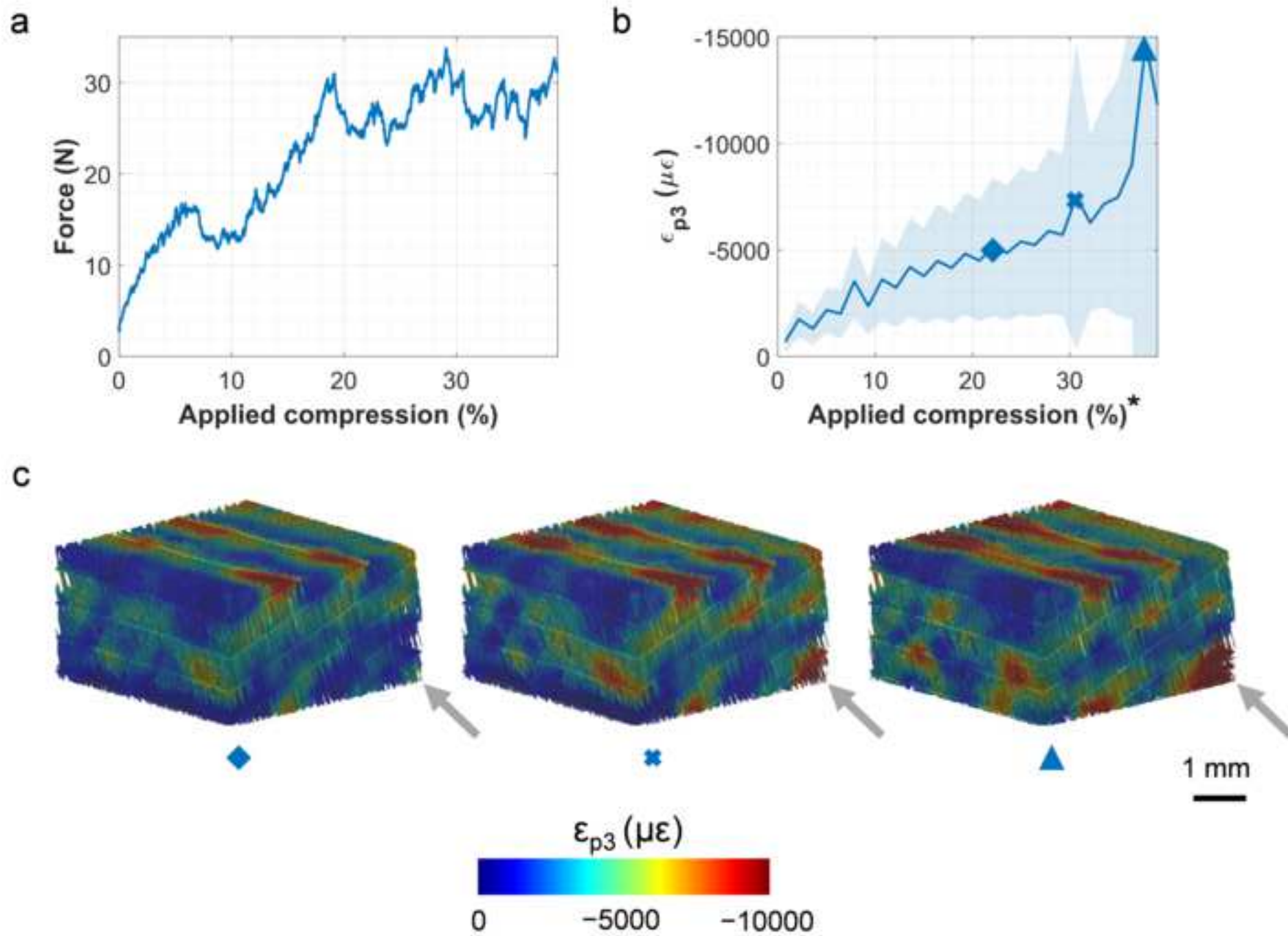


Figure9.png













Click here to access/download
Supplementary Material
SupplementaryMaterial_Rev1.pdf





Click here to access/download
Supplementary Material
VideoS1.avi






Click here to access/download
Supplementary Material
VideoS2.avi






Click here to access/download
Supplementary Material
VideoS3.avi





Click here to access/download
Supplementary Material
VideoS4.avi





Click here to access/download
Supplementary Material
VideoS5.avi



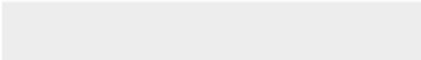



Click here to access/download
Supplementary Material
VideoS6.avi





Click here to access/download
Supplementary Material
VideoS7.avi





Click here to access/download
Supplementary Material
VideoS8.avi



Declaration of interests

The authors declare that they have no known competing financial interests or personal relationships that could have appeared to influence the work reported in this paper.

The authors declare the following financial interests/personal relationships which may be considered as potential competing interests:

F.W. is an employee of Biotrics Bioimplants AG which partially funded this study. The remaining authors declare that they have no known conflict of interests.